Tectonophysics 601 (2013) 37–52

Contents lists available at SciVerse ScienceDirect

Tectonophysics

journal homepage: www.elsevier.com/locate/tecto

The role of a hidden fault in stress triggering: Stress interactions within the 1935 *Mw* 7.1 Hsinchu–Taichung earthquake sequence in central Taiwan

Den-Hor Lin [a,1], Kate Huihsuan Chen [b,2], Ruey-Juin Rau [c,*], Jyr-Ching Hu [d,3]

[a] Center for General Education, Cheng Shiu University, Kaohsiung, Taiwan
[b] Department of Earth Sciences, National Taiwan Normal University, Taipei, Taiwan
[c] Department of Earth Sciences, National Cheng Kung University, 1 University Rd., Tainan 701, Taiwan
[d] Department of Geosciences, National Taiwan University, P.O. Box 13-318, Taipei 106, Taiwan

ARTICLE INFO

Article history:
Received 11 September 2012
Received in revised form 14 April 2013
Accepted 19 April 2013
Available online 28 April 2013

Keywords:
Stress interactions
Earthquake triggering
Blind fault
The 1935 *Mw* 7.1 Hsinchu–Taichung earthquake
Earthquake hazard

ABSTRACT

Hidden faults often lead to misestimation of earthquake hazard. In western Taiwan where many blind faults are located, how the stress interactions correlate with potentially significant earthquakes and what is the role of blind faults in earthquake triggering are the important questions for earthquake hazard assessment. Given sequential rupture of active faults with an unexposed fault segment involved, the 1935 *Mw* 7.1 Hsinchu–Taichung earthquake sequence in central Taiwan provides an exceptional case to study. This destructive earthquake sequence took ~3000 lives and was composed of four $M > 6$ earthquakes occurred within three months. The *Mw* 7.1 mainshock and a subsequent *Mw* 6.8 event that occurred 12 s later caused surface ruptures on the Tuntzuchiao fault (TTCF) and Shihtan fault (STF) which are separated by 25 km. These two ruptures were characterized by different types of faulting: thrust-faulting on the STF and right-lateral faulting on the TTCF fault. About 24 min later, an *Mw* 6.0 event occurred ~45 km north of the mainshock. Three months later on July 17, the last event, *Mw* 6.2, occurred 30 km northwest of the mainshock. In this study we revisit the data available for the 1935 sequence in an effort to place constraints on the fault models. Using five different fault models, a series of Coulomb stress calculations are conducted to understand whether static stress transfer advances slip during the subsequent events. We propose that key features of the 1935 Hsinchu–Taichung earthquake triggering can be explained by the existence of an unexposed fault segment in between the segments of TTCF and STF. We also show that the 1935 earthquake sequence may play an important role in activating post-1935 earthquake activity along the Sanyi–Puli seismic zone, where the sequential ruptures of the 1935 events encourage ruptures of a NW–SE-trending seismic zone at later times.

1. Introduction

The 1935 *Mw* 7.1 Hsinchu–Taichung earthquake was the most destructive sequence to strike central Taiwan in the last century and caused the death of more than 3000 people. This event occurred near the 1999 *Mw* 7.6 Chi-Chi source region and was the largest historic event prior to the Chi-Chi earthquake in Taiwan. The 1935 mainshock is known to cause two fault ruptures that are ~20 km apart. Unexposed ruptures in between these two faults are suspected to be active during the 1935 sequence (Otuka, 1936), yet there is no enough data/information to support this possibility on the role of buried faults in earthquake triggering.

The 1935 earthquake sequence is composed of four $Mw > 6$ strike-slip and thrust faulting events as shown in Fig. 1 and Table 1. The *Mw* 7.1 mainshock had an epicenter of 24.35°N, 120.82°E (event No. 1 in Fig. 1) with a focal depth of less than 10 km (TMO, Taipei Meteorological Observatory, 1936), which created a 12-km-long surface rupture on the Tuntzuchiao fault (TTCF) (Otuka, 1936). Within twelve seconds, an *Mw* 6.8 event (event No. 2 in Fig. 1) occurred 25 km north of event No. 1 (Lin, 1987) and ruptured along the 15-km Shihtan fault (STF) (Otuka, 1936). An *Mw* 6.0 followed 24 min later and located ~45 km north of the mainshock, near the Chungkang River (event No. 3 in Fig. 1). Three months later this sequence was completed by an *Mw* 6.2 event on July 17, located 30 km northwest of the mainshock near the Houlung River (event No. 4 in Fig. 1). Consequently, this sequence was composed of four $Mw > 6$ events and two surface ruptures within 3 months.

This sequence occurred on the active fold-thrust belt in western foothills of Taiwan, along the western portion of the Taiwan orogen. The belt is a result of ongoing oblique collision between the Luzon arc of the Philippine Sea plate and the Chinese continental margin of the Eurasian plate (Suppe, 1981; Teng, 1990). The relative motion

* Corresponding author at: Department of Earth Sciences, National Cheng Kung University, Tainan 701, Taiwan. Tel.: +886 6 2757575 65425; fax: +886 6 2740285.
E-mail addresses: kuo328j@yahoo.com.tw (D.-H. Lin), katepili@gmail.com (K.H. Chen), raurj@mail.ncku.edu.tw (R.-J. Rau), jchu@ntu.edu.tw (J.-C. Hu).
[1] Tel.: +886 7 731 0606x6490.
[2] Tel.: +886 2 7734 6400.
[3] Tel.: +886 2 2363 4860.

0040-1951/$ – see front matter © 2013 Elsevier B.V. All rights reserved.
http://dx.doi.org/10.1016/j.tecto.2013.04.022

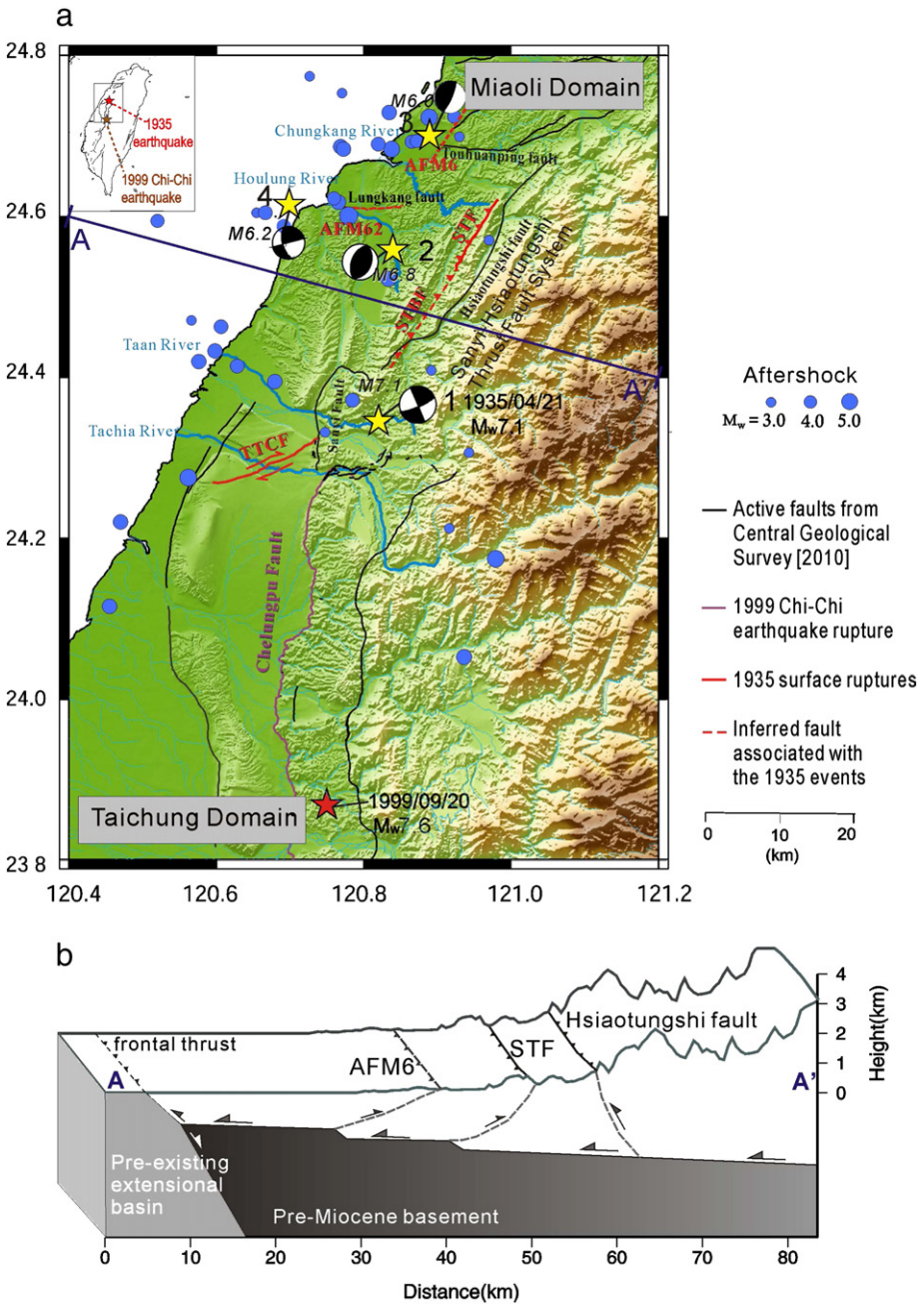

Fig. 1. (a) Tectonic map of the study area (Miaoli Domain) and distribution of major earthquakes during the 1935 Hsinchu–Taichung earthquake sequence in the northwest of Taiwan. The major events in the 1935 earthquake sequences are denoted by different numbers and focal mechanisms (detailed information are shown in Table 1). Blue circles indicate the $3.0 \leqq M < 6.0$ aftershocks that occurred during the period of April 21 to July 20, 1935 (TMO, Taipei Meteorological Observatory, 1936; relocated by Lai et al., 2004). Red stars denote the epicenter of the 1935 *Mw* 7.1 and the 1999 *Mw* 7.6 Chi-Chi mainshock. Ruptured faults during the 1935 and 1999 earthquake sequences are shown by red and purple lines, respectively. Dash red lines denote the fault segment corresponding to the major 1935 events without notable surface rupture evidence (inferred fault). Active faults from the Central Geological survey are indicated by black lines. TTCF, Tuntzuchiao fault; STF: Shihtan fault; STBF: Shihtan-Tuntzuchiao blind fault; AFM6: The fault plane of the *Mw* 6.0 aftershock (06:26, April 21, 1935); AFM62: The fault plane of the *Mw* 6.2 aftershock (July 17, 1935). (b) Schematic structural model for cross-section A–A' (modified from Lin, 2005).

between the two plates is about 8.2 cm/yr in the direction normal to the strike of the fold-thrust belt (N315°; Seno et al., 1993; Yu et al., 1997). Two major seismic faults ruptured during the 1935 earthquake sequence: 1) The TTCF corresponding to the *Mw* 7.1 mainshock (event No.1 in Fig. 1). This fault is located in a transition zone between the Taichung and Miaoli tectonic domains of Taiwan, which serves as an accommodation structure within a fold-and-thrust belt (Shyu et al., 2005). 2) The STF corresponding to the *Mw* 6.8 aftershock (event No. 2) located ~25 km north of TTCF near the eastern end of the Houlung River. It is considered as a back thrust parallel to the major east-dipping thrust faults in western Taiwan, such as the Sanyi-Hsiaotungshi Thrust Fault System and the Chelungpu Fault (Hukunaga and Sato, 1938; Lin et al., 2000; Miyabe et al., 1938) (Fig. 1). Back thrusts usually play an important role in the deformation of the western foothills, which accommodates the crust shortening to generate earthquakes (e.g., Lee et al., 2002). The major surface ruptures transformed from right-lateral faulting on the TTCF to thrust-faulting on the STF, where some buried fault segments between these two faults were suggested (Otuka, 1936). Due to the complex fault system in this area and thus various fault models proposed, there is no compelling

Table 1
Parameters of mainshock and larger aftershocks (*Mw* ≧ 6) of the 1935 Hsinchu–Taichung earthquake sequence.

Date/time (Local time)		Hypocenter (lon., lat., dep.)		Strike	Dip	Rake	Magnitude (*Mw*)	References
April 21, 1935	06:02:00	120.82°E, 24.35°N	3.0 km	67°	80°	180°	7.1	TMO, Taipei Meteorological Observatory (1936); ERI, Earthquake Research Institute (1936); Sheu et al. (1982); Cheng (1995); Chen and Tsai (2008)
April 21, 1935	06:02:12	120.84°E, 24.56°N	6.0 km	203°	50°	90°	6.8	Sheu et al. (1982); Lin (2005)
April 21, 1935	06:26:00	120.89°E, 24.70°N	3.0 km	203°	10°	90°	6.0	Lin (1987); Chen and Tsai (2008)
July 17, 1935	00:19:00	120.68°E, 24.60°N	20.0 km	165°	60°	0°	6.2	TMO, Taipei Meteorological Observatory (1936); Huang and Yeh (1992); Cheng (1995; Chen and Tsai (2008)

model for stress triggering between the 1935 events. One therefore needs to examine Coulomb stress changes on both active and buried faults, to understand their relative change in failure potential.

Calculation of static Coulomb stress change is commonly used to understand earthquake interactions, which may explain aftershock distribution, changes in seismicity rate and the advance or delay of subsequent major earthquakes (e.g., Dieterich, 1994; Harris, 1998; King et al., 1994; Stein, 1999). An increase in Coulomb stress change is found to explain off-fault aftershocks in a few mainshock rupture lengths (Das and Scholz, 1981; Oppenheimer et al., 1988; Smith and Van de Lindt, 1969; Stein and Lisowski, 1983), while dynamic stress due to passage of seismic waves can explain distant triggered seismicity and asymmetry in aftershock locations (e.g., Anderson et al., 1994; Gomberg and Bodin, 1994; Gomberg et al., 1997, 2000, 2001; Hill et al., 1993; Voisin et al., 2004). At short distance from the mainshock such as the 1935 case, however, static and dynamic triggering processes both are likely responsible for elevated seismicity and aftershocks (Gomberg et al., 2003; Kilb, 2003; Kilb et al., 2000; Voisin et al., 2004). Computation of dynamic stress changes requires sufficient records of seismograms, which is a difficult task for the study of the 1935 event. Here we only consider the role of static stress triggering in the 1935 earthquake sequence.

Unlike strike-slip fault systems, stress transfer pattern in thrust systems is more variable with depth (e.g., Lin and Stein, 2004), which complicates interpretations of stress interactions. In the western foothills of Taiwan where many blind faults are located, the role of stress interactions among major earthquakes and the role of blind faults in earthquake triggering are the crucial topics for earthquake hazard assessment. It is still unknown whether an unexposed STF fault segment influenced the fault interaction process during the 1935 sequence. Can the static stress triggering explain the occurrence of the second mainshock rupture (STF) and the *Mw* 6 aftershocks? What is the role of blind faults on earthquake triggering in this particular region? In this study we revisit the data available for the 1935 earthquake sequence in an effort to place constraints on the nature of sequential ruptures, so as to model stress interaction between the sequential ruptures of the 1935 Hsinchu–Taichung earthquake sequence.

2. Observations of *Mw* 7.1 mainshock

2.1. Field investigation

Field investigation of the 1935 surface ruptures shows a fault length of 12 km (ERI, Earthquake Research Institute, 1936) and 15 km (Otuka, 1936) for the TTCF and STF, respectively (Model A in Fig. 2a, Table 2). The STF is a thrust fault with strike of N30°E that exhibited 0.3–3 m vertical offset (Otuka, 1936), whereas TTCF is an oblique fault with the strike of N60°E that revealed maximum displacement of 1.6 m. Several minor surface faults, landslides, and fissures were evidently found in between the two major ruptures, suggesting that parts of the TTCF and STF were probably unexposed (Otuka, 1936).

2.2. Geodetic measurements and models

Using the 1917–1937 triangulation and leveling data (Military Land Survey, 1937) that contain 58 points covering the entire study area, Sheu et al. (1982) optimized a model to obtain a fault length of 35 km for the STF, which is about 3 times longer than that revealed from surface observations, and a fault length of 20 km obtained for the TTCF is also longer than the observed surface rupture (Model B in Fig. 2b, Table 2). Note that only two rectangular fault segments were considered in their study with equal width of 10 km. The strike, dip, rake, fault width, average slip for STF and TTCF are (N23°E, 50°W, 90°, 10-km, 2-m) and (N67°E, 80°E, 180°, 10-km, 1.5-m), respectively (Fig. 2b, Table 2).

Other than a simple rectangular fault model (Sheu et al., 1982), Huang and Yeh (1992) conducted a finite-element model with more complicated fault geometries to fit the same geodetic data. They found that heterogeneous slip with more complex fault geometry is needed to fit the observations. A listric fault is proposed for the STF with dip angle varying from 55° near the surface to 30° at the bottom of the fault. The TTCF bends from N70°E to N55°E, from the west to the east end of the fault (Model C in Fig. 2c, Table 2). Additionally, the fault model for the *Mw* 6.2 aftershock (No. 4 in Fig. 1) is inferred to have strike N15°W, dip angle 60°W, rake 0°, and slip 1 m. The transformation from the strike-slip faulting on the TTCF to reverse faulting on the STF indicates complex rupture process during the 1935 earthquake sequence.

Taking geomorphological evidences into account, Lin (2005) used multiple segments of faults to fit the triangulation data (Military Land Survey, 1937). Other than a pre-existing normal fault to the east of the TTCF, two more unexposed STF segments were considered extending from the STF surface ruptures in the north to the east end of the TTCF (Model D in Fig. 2d, Table 2).

2.3. Seismic data

The 1935 earthquake sequence was recorded by nine analog seismic stations in Taiwan (see Fig. S1 in the Supplementary material). They were equipped with three-component low-gain displacement seismometers. In the earthquake catalogs provided by TMO (Taipei Meteorological Observatory) (1936), major earthquakes were located using S minus P times and are shown by blue circles (Fig. 1a).

Using a total of 22 P-wave first motion records in western Pacific stations, Sheu et al. (1982) determined focal mechanism of the mainshock as right-lateral strike slip faulting with the strike N45°E and dip angle 83°E, which is consistent with the TTCF rupture. The next major event in the TMO catalog is the M_L 6.0 event (No. 3 in Fig. 1a), which is too small to accompany a surface rupture of 15 km in STF (see Section 2.1). A seismic event corresponding to the STF rupture remained missing until the source rupture process research conducted by Lin (1987). In his work waveforms from six seismic stations were scanned, digitized, detrended, and the skewness of the traces was corrected and the instrument response was removed. By visual inspection, he noted an early aftershock signal concealed inside the mainshock coda (Fig. S2 in the Supplementary material). The first rupture occurred 12 s ahead of the second one. The early aftershock was picked from the mainshock seismogram and inferred as thrust faulting,

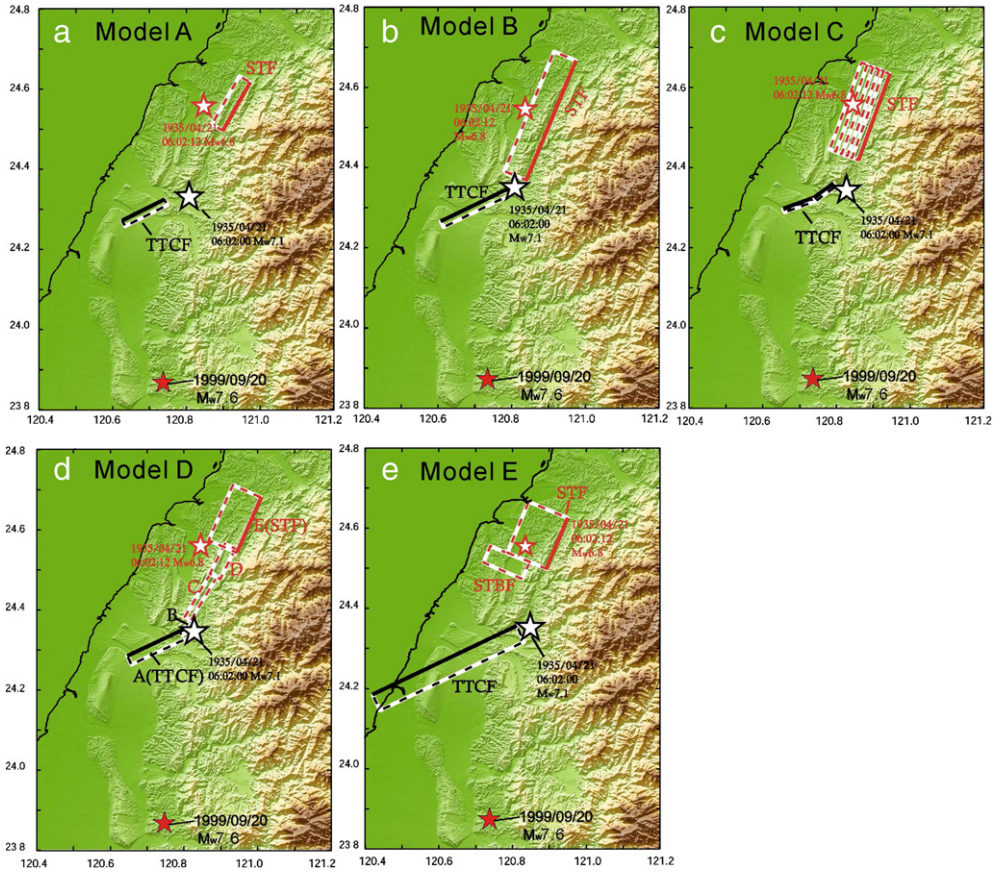

Fig. 2. Illustration of fault models (A–E) in Table 2. The 1999 *Mw* 7.6 Chi-Chi mainshock is shown as the red star. The 1935 *Mw* 7.1 Hsinchu–Taichung mainshock and its *Mw* 6.8 aftershock are shown as white stars (see Table 2 for the explanations of each fault segment in each fault model).

Table 2
Fault models of TTCF and STF.

Model		Strike	Dip	Rake	L (km)	W (km)	Max. slip (m)	Cal. *Mw*	Obs. *Mw*	References	Data
A	TTCF	60°	X	X	12	10.0	1.6	6.4	7.1	Otuka (1936)	F
	STF	210°	X	X	15	10.0	3.0	6.7	6.8	Otuka (1936)	F
B	TTCF	67°	80°	180°	20.0	10.0	1.5	6.6	7.1	Sheu et al. (1982)	T
	STF	203°	50°	90°	35.0	10.0	2.0	6.8	6.8	Sheu et al. (1982)	T
C	TTCF	55–70°	80–85°	180°	15.0	6.2	1.9	6.4	7.1	Huang and Yeh (1992)	T
	STF	200°	30–55°	90°	25.0	11.0	1.94	6.7	6.8	Huang and Yeh (1992)	T
D	TTCF (A)	63°	80°	139°	18.0	15.0	1.57	6.8	7.1	Lin (2005)	T
	TTCF (B)	42.6°	85°	−148°	5.2	12.0	5.45			Lin (2005)	T
	STBF (C)	211°	75°	123°	14.0	7.5	2.49	6.9	6.8	Lin (2005)	T
	STBF (D)	206.5°	65°	−146°	9.0	7.5	3.43			Lin (2005)	T
	STF (E)	203°	45°	161°	16.0	11.7	3.84			Lin (2005)	T
E	TTCF	67°	80°	180°	40.2	27.7	2.2	7.1	7.1	Lin (2005)	T
	STBF	203°	40°	90°	5.0	15.0	2.4	6.8	6.8	Lin (1987)	S
	STF	203°	40°	90°	15.0	15.0	2.8			Lin (1987)	S

TTCF: Tuntzuchiao surface fault.
STF: Shihtan surface fault.
AFM6: The fault plane of the M_w 6.0 aftershock (Event 3 in Fig. 1).
AFM62: The fault plane of the M_w 6.2 aftershock (Event 4 in Fig. 1).
STBF: Shihtan blind fault between TTCF and STF in Model C.
L: Fault length.
W: Fault width.
H.Slip: Horizontal slip (positive for right-lateral fault).
V.Slip: Vertical slip (positive for reverse fault).
Seismic moment: $M_0 = \mu DLW$ ($\mu = 2.5 \times 10^{11}$ dyn/cm^2, D: fault slip, L: fault length, W: fault width).
F: Field.
T: Triangulation.
S: Seismogram.

which is consistent with the STF rupture. It is reasonable therefore, to link the second event (No. 2) to the STF rupture. By comparing the observed and computed waveforms, he also determined the fault length and width of the STF to be 20.14 km and 15 km, respectively, equivalent to an *Mw* 6.8 earthquake (Model E in Fig. 2e, Table 2).

3. Observations of *M* 6 aftershocks

After the mainshock, two *Mw* 6.0 aftershocks hit the coastal area as denoted by events No. 3 and 4 in Fig. 1. There was no evidence of surface rupture during the 1935 earthquake sequence near the *Mw* 6.0 epicentral area (Chungkang and Houlung Rivers). The focal mechanisms, geodetic data, and spatial correlation to the local fault segments suggest that the No. 3 and No. 4 events are likely associated with the Touhuanping and Lungkung faults, respectively (Huang and Yeh, 1992; Miyabe et al., 1938). A fault length of 5 km for the April 21 *Mw* 6.0 aftershock fault plane (strike = 203°, dip = 10°, rake = 90°) was obtained by Lin (1987) using the simulation of strong motion waveforms. He proposed an additional fault segment in the northeast of the major ruptures, called AFM6, corresponding to the *Mw* 6.0 aftershock (06:26, April 21, 1935). The No. 4 event fault plane is considered as the conjugate faulting with the TTCF due to the same regional stress (Huang and Yeh, 1992). The fault plane solution of No. 4 event (referred as AFM62 in Table 3) is either a sinistral strike-slip fault (strike = 165°, dip = 60°, rake = 0°) or a dextral strike-slip fault (strike = 75°, dip = 90°, rake = 150°), according to the fit of geodetic data (Huang and Yeh, 1992). The stresses solved on both fault planes of No. 4 event are considered in our following stress computation.

4. Fault models

4.1. Models A–E

In Model A the fault geometries and maximum slip of TTCF and STF are derived from surface investigation, as indicated by Model A in Table 2. Fault width of 10 km is assumed to be the same as the value obtained from triangulation data (Sheu et al., 1982) in Model B. Fig. 2a displays the fault model in mapview. Assuming a fault width of 10 km, the equivalent earthquake magnitudes for TTCF and STF ruptures are *Mw* 6.4 and 6.7, respectively, which are smaller than the actual magnitude *Mw* 7.1 and 6.8, respectively.

In Models B to D the fault geometries and average slips are determined using triangulation and leveling data provided by Sheu et al. (1982), Huang and Yeh (1992), and Lin (2005). The models vary from the simple two-rectangular segments, a listric segment with non-uniform slip, to the multiple segments models, as shown in Fig. 2b–d. Fault parameters of TTCF and STF for the following Coulomb stress computation are listed in Table 2.

Fault model constrained by seismic data from Lin (1987) is inferred as Model E (Fig. 2e), where the fault parameters of No. 2 (STF and STBF ruptures) and No. 3 events are determined by the seismic data inversion, as listed in Table 2 and Table 3. The focal mechanisms determined from the 6 stations are shown in Fig. S3 of the Supplementary material (Lin, 1987). In Model E an additional blind fault extending southwards from the 15-km-long surface rupture of STF is adopted. This unexposed segment is called the Shihtan blind fault (STBF) in Model E of Table 2, where the total fault length is constrained by the cumulative seismic moments along the STF by Lin (1987), to meet the observed *Mw* 6.8.

Blind faults are considered in Models D and E: The STF is divided into a blind segment and a surface breaking segment with different amount of slip in Model E, whereas two blind segments, one surface breaking segment are used in Model D. Table 2 lists the details of modeling parameters considered in the following stress computation.

4.2. Determination of moment magnitude

We used the moment magnitude (*Mw*) taken from the "Taiwan 1900–2006 earthquake catalog" provided by Chen and Tsai (2008), where they obtained moment magnitude *Mw* using (1) empirical relations between Hsu's magnitude M_H, duration magnitude M_D, and local magnitude M_L and (2) the best-fitting a- and b-values. Here the Hsu's magnitude M_H was corrected from surface-wave magnitude by Hsu (1971) as shown in Eq. (1), whereas M_D is determined by signal duration in the form of Eq. (2). Local magnitude M_L is measured by maximum amplitude of the displacement seismograms as the amplitude–distance curve in Yeh et al. (1982).

$$M_H = \log A + 1.09\log\Delta + 0.50 \tag{1}$$

$$M_D = -0.87 + 2.00\log D + 0.0023\Delta + R \tag{2}$$

In Eqs. (1) (Hsu, 1971) and (2) (Shin, 1986), A, Δ, D, and R represent maximum trace amplitude, epicentral distance, signal duration, and station correction in a range of −0.01–0.45, respectively.

For the No. 2 event that was missing in their catalog, we used the empirical relationship below to determine *Mw*. The seismic moment (M_o) is inferred by Lin (1987) from seismic data (Hanks and Kanamori, 1979).

$$M_w = \frac{2}{3}\log(M_0) - 10.7 \tag{3}$$

The calculated seismic moment of TTCF for Models A to D are 4.8×10^{18}, 7.5×10^{18}, 4.4×10^{18}, 1.9×10^{18} N-m, equivalent to the *Mw* 6.4, *Mw* 6.6, *Mw* 6.4, and *Mw* 6.8 events, respectively. They are much smaller than the mainshock magnitude *Mw* 7.1 due to the fault length less than 20 km in the models. Therefore in Model E we attempt to increase the fault length and width to meet the observed magnitude. The calculated seismic moment of STF alone in Models A–C and the blind STF segments considered in Models D–E are 1.1×10^{19}, 1.8×10^{19}, 1.3×10^{19}, 3.0×10^{19}, and 2.0×10^{19} N-m, equivalent to the *Mw* 6.7, *Mw* 6.8, *Mw* 6.7, *Mw* 6.9, and *Mw* 6.8 events, respectively, which approximately equivalent to the observed magnitude, *Mw* 6.8 (No. 2 event). The biggest seismic moment produced by Model D is due to the longest fault length of STF, 39 km, which accounts for one surface breaking segment and two unexposed segments.

Data were insufficient for the determination of the two *M* 6 aftershock fault models. The fits of seismic data by Lin (1987) provided a fault model named AFM6, corresponding to No. 3 event, whereas the fits of geodetic data (Huang and Yeh, 1992) provided a fault model named AFM62, corresponding to No. 4 event. Fault parameters listed in Table 3 are used in the stress computations for M6 aftershocks.

Table 3
Fault models of *M* 6 aftershocks used for Models A–E.

	Strike	Dip	Rake	L (km)	W (km)	Av. slip (m)	Cal. *Mw*	Obs. *Mw*	References	Methodology
No. 3 (AFM6)	203° 23°	10° 80°	90° 90°	5.0	8.0	1.2	6.0	6.0	Lin (1987)	Seismogram
No. 4 (AFM62)	165° 75°	60° 90°	0° 150°	12.5	5.8	1.0	6.2	6.2	Huang and Yeh (1992)	Triangulation

5. Coulomb stress change

Calculation of static Coulomb stress can help us to understand stress interaction process and to explain the evolution of seismicity patterns (e.g., Harris, 1998; Stein, 1999). The static Coulomb stress changes (ΔCFS) are calculated by

$$\Delta CFS = \Delta\tau + \mu(\Delta\sigma - \Delta P), \quad (4)$$

where Δτ is the shear stress change along the slip direction on the assumed fault plane, μ is the coefficient of friction, Δσ is the normal stress change, and ΔP is the change in pore fluid pressure. The Coulomb stress changes are calculated at the centers of 1.0 km × 1.0 km cells using the methods and Coulomb 3.0 software described in Toda et al. (2005). We computed stress changes on receiver planes due to rectangular dislocations in a uniform, elastic half-space with a Poisson's ratio of 0.25 and shear modulus of 3.3×10^4 MPa. The required input for the program computation are fault location, length, width, dip angle, the amount of slip on the fault, and the receiver fault orientation. Laboratory experiments show that at slow slip rates ($\ll 1$ m/s), μ appears to be in a range of 0.6–0.9 for almost all rock types (Byerlee, 1978). For a strike-slip fault, μ is commonly considered to be low (e.g., 0.4), whereas for a continental thrust μ is generally higher (up to 0.8) (King et al., 1994). Lower apparent coefficient of friction could occur if the fault has been experiencing more cumulative slip (Parsons et al., 1999). However, using the covariation of topography (surface slope) with detachment dip, Suppe (2007) proposed a much weaker μ, 0.04–0.1, on the basalt detachment of Taiwan. To simplify the computation, we perform tests with a wide range of μ to assess the robustness of the model E in Fig. 3. The sensitivity test shows that Coulomb stress lobes induced by the TTCF rupture

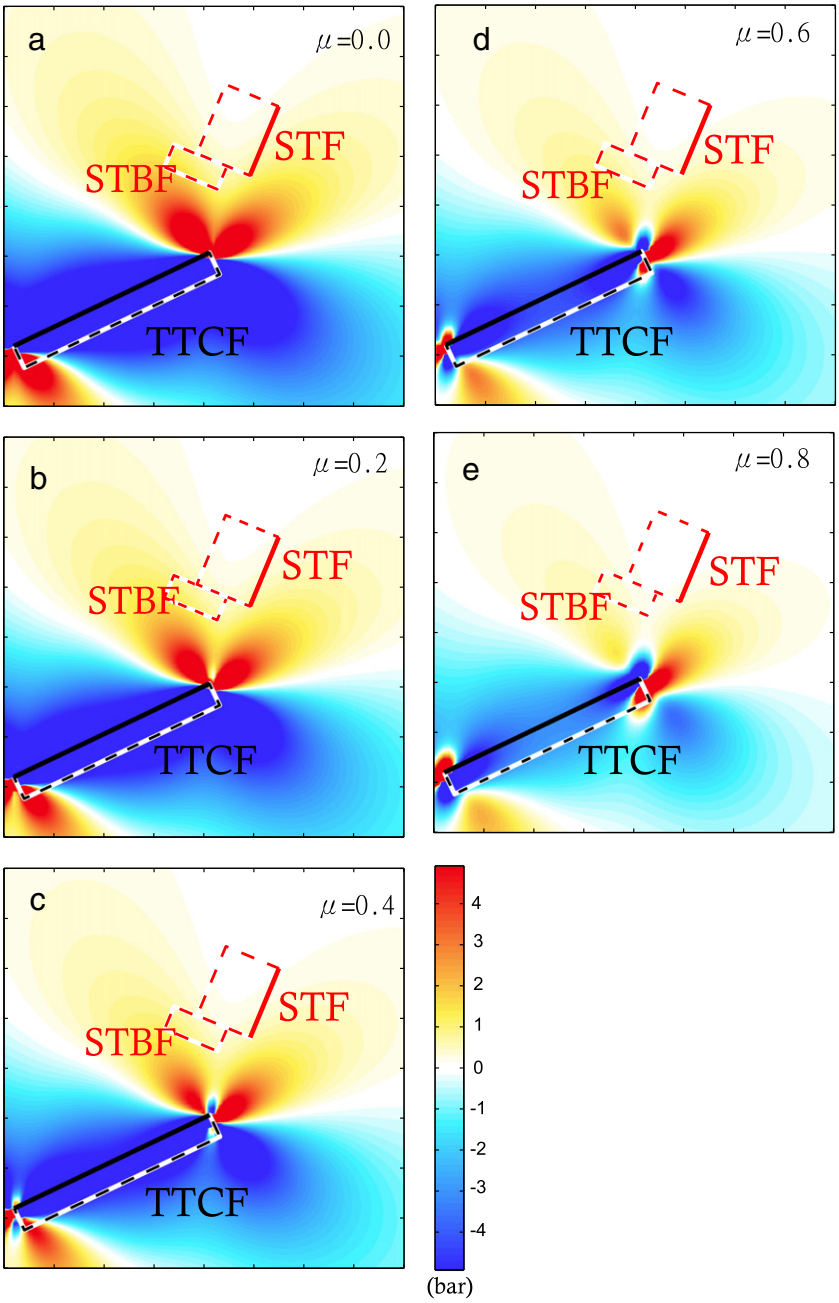

Fig. 3. Sensitivity analysis of stress change computation at a depth of 6 km using STBF + STF as the receiver fault, with μ ranging from 0.3 to 0.8. Black and red lines denote the fault model for stress calculation in Model E (detailed fault parameters are shown in Table S1 of the Supplementary material).

(Fig. 3) remain highly similar; suggesting the influence of the choices of μ on the stress change pattern is modest. The regional stress direction in the northwestern Taiwan is NW–SE (e.g., Angelier et al., 1986; Hu et al., 1996) with an azimuth of 315°, which is used in our stress computation as the regional stress axes.

We also examined the effects of varying strike, dip angle, and rake on stress induced by the TTCF rupture. Values of strike, dip and rake span the range of plausible values listed in Table 2 for the source model, approximate the maximum and minimum values of the TTCF model. Instead of the visual comparison, we report maximum Coulomb stress changes on the receiver fault in Fig. 4. The sensitivity tests indicate that the computed stresses are in a range of 0.3 bars while the values are in the same stress triggering lobes except for small rake (130°) from Model D. The rake has to be greater than 160° to enforce the same polarity of stress change. Note that in the five fault models, only Model D constrained by the geomorphology data revealed a rake = 139° while others shows a rake = 180°. The relationship between the next rupture location and the stress change, therefore, is shown to be insensitive to the selected range of μ = 0.4–0.8, fault length = 10–30 km, fault width = 10–30 km, strike = 50°–80°, dip angle = 60°–90°, and rake = 160°–180°.

Most studies on static Coulomb stress calculation have been applied on strike-slip fault systems (Dieterich and Kilgore, 1996; Harris and Simpson, 1998; Stein et al., 1997; Toda and Stein, 2003; Toda et al., 2005), where the Coulomb stress change does not vary greatly with depth. In the thrust fault systems, however, the depth-dependent stress field may complicate the stress interaction between faults (Lin and Stein, 2004). A surface-cutting thrust fault relieves stress over a wide area in the cross-section, inhibiting failure on nearby thrust faults. In contrast, blind thrust faults may increase the stress toward failure in the overlying crust that produces broadly distributed aftershocks (Lin and Stein, 2004; Toda, 2008), which may pose unexpected seismic hazard.

The 1935 Hsinchu–Taichung earthquake sequence is composed of the sequential surface ruptures of TTCF and STF induced by the *Mw* 7.1 mainshock and two *Mw* > 6.0 aftershocks. To explain the spatio-temporal distribution of large earthquakes during the 1935 Hsinchu–Taichung earthquake sequence, we next compute the stress evolution at successive rupture sites by sequential plots of the Coulomb stress change.

6. Stress evolution results using different fault models

A visual comparison of computed Coulomb stress changes using five different fault models is discussed in this section. Using Models A, B, and C the static stress change caused by the mainshock rupture (TTCF) on STF are shown in Fig. 5a–c, where the STF does not fall into the region where positive Coulomb stress changes in a range of −0.09 to −0.17 bars. This suggests that the stress triggering derived from this fault model is unlikely to explain the STF rupture. In Models D and E where the unexposed segment(s) are considered, the stress imparted near the STF is positive, between 0.02 and 5.5 bars (Fig. 5d–e). This indicates that the controlling factor of triggering between TTCF and STF lies on the difference between Models A–C and Models D–E. The derived stress change implies that the existence of a blind fault likely played a significant role in triggering the STF rupture.

The stress evolution at successive rupture sites using five different fault models (Models A to E in Table 2) is illustrated by the sequential

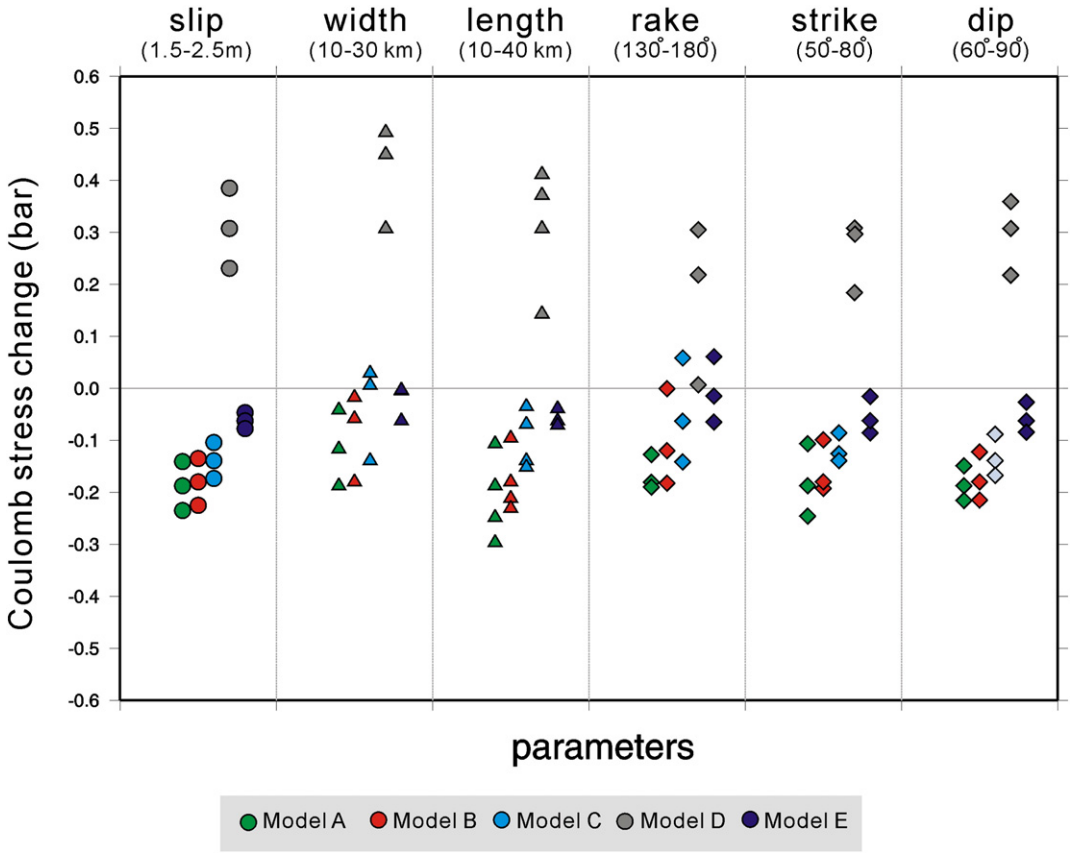

Fig. 4. Sensitivity analysis of stress change computation on STF, with varying slip, fault width, fault length, rake, strike, and dip angle. The range of parameters approximates the maximum and minimum values of the TTCF fault models in Table 2. Circle, triangle, and diamond represent the sensitivity test by changing slip (meter), length (kilometer), and angle (degree). Source model is based on TTCF in Model E (strike 67°, dip 80°, rake 180°), whereas receiver fault is STBF + STF (strike 203°, dip 40°, rake 90°).

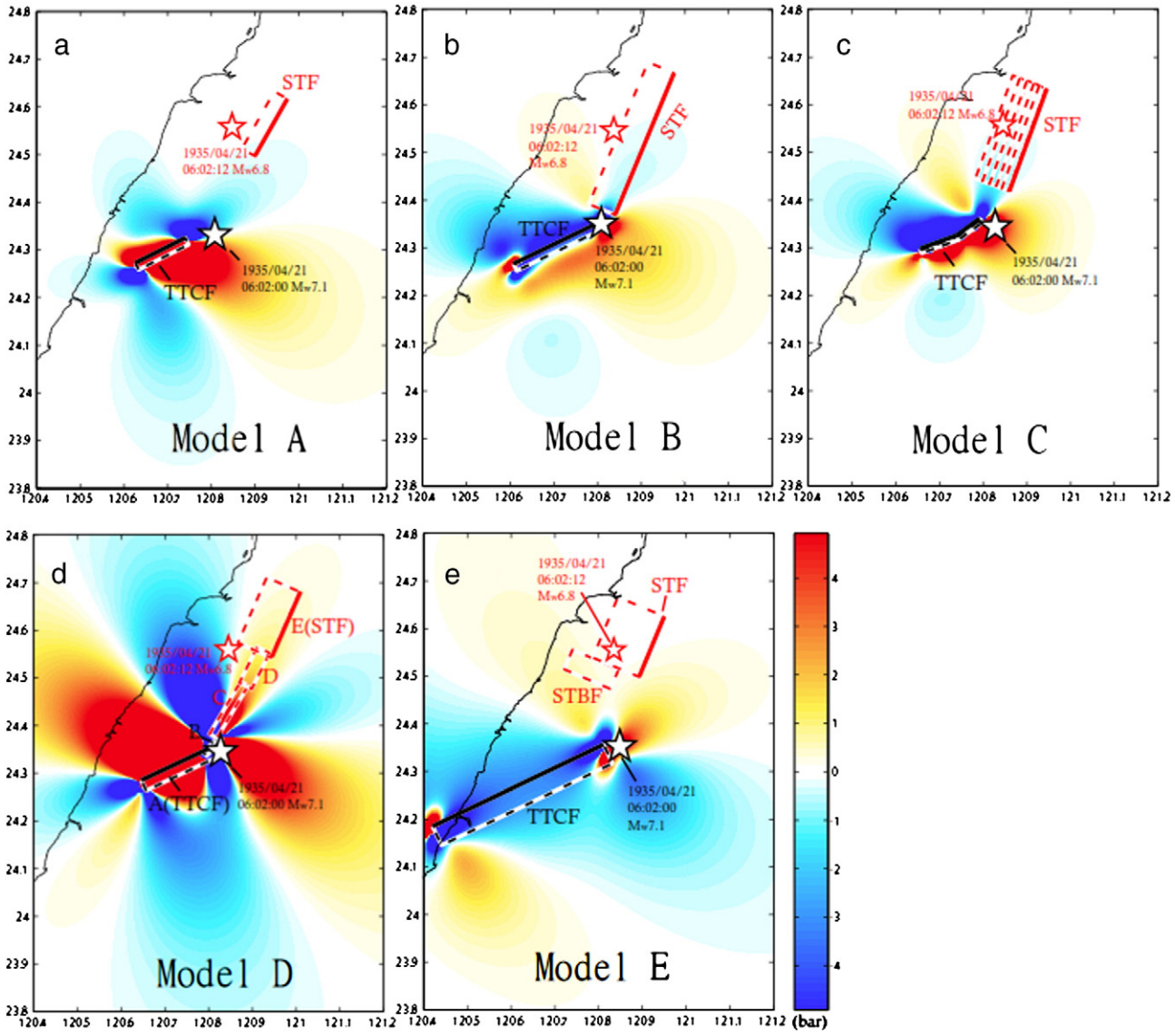

Fig. 5. Coulomb stress changes caused by the TTCF rupture using the five fault models in Table 2, assuming $\mu = 0.4$. The Coulomb stress changes are resolved at a depth of 6 km. Black line denotes the fault model for stress calculation. Red line denotes the next rupture.

plots of the Coulomb stress change in Figs. 6–10. In Fig. 6a–b we first calculated the Model A derived static stress changes on the STF, where the STF is unlikely to fall in the region where the stress increased. The stress changes caused by the combined effect of the TTCF and STF ruptures on the subsequent *Mw* 6.0 event are shown in Fig. 6c–d. As indicated in the cross section, the subsequent April 21 *Mw* 6.0 event is located in the stress shadow zone. A combined effect of the previous two ruptures and the *Mw* 6.0 event on the *Mw* 6.2 event (which occurred 3 months later) is shown in Fig. 6e–h, where the subsequent rupture is in the negative stress change region. The other fault plane for the last event (AFM62 model) is computed in Fig. 6g–h, resulting in a similar pattern with Fig. 6e–f.

Stress evolution using Models C and D is shown in Figs. 7 and 8. The bended TTCF and listric STF in Model D reveal more complicated geometry than the rectangular models assumed in Model C. The stress changes due to sequential ruptures are found to occur in the stress increased zone except for the STF rupture. The stress patterns generated by these two models are very similar. This indicates that the more complicated fault geometry does not change the stress field much.

Unexposed STF is considered in Models D and E. We first calculate the static stress changes caused by the TTCF on both the STF and the blind fault plane STBF (Figs. 9 and 10). In Model D where the two unexposed STBFs are considered, the Coulomb stress changes on STF(C), STBF(D), and STBF(E) segments are 5.5, 1.8, and 0.5 bars, respectively (Fig. 9a–b). In Model E with only one unexposed STBF, the stress changes on STF and STBF segments are 0.4 and 0.03 bars, respectively (Fig. 10a–b). This suggests that the faulting of TTCF may have brought the STBF(s) and STF closer to failure. The combined effect of the TTCF, STBF(s), and STF faulting on the fault plane of AFM6 is shown in Fig. 9c–d and Fig. 10c–d, where the next AFM6 rupture is located in the positive stress change zone (3.4 and 4.4 bars). The ensuing *Mw* 6.2 event lies within a region of stress shadow, assuming the fault plane of AFM62 as strike = 165°, dip = 60°, and rake = 0° (Fig. 9e–f and Fig. 10e–f), whereas the *Mw* 6.2 event lies in a stress increased zone in Model D when the other fault plane is assumed (Fig. 9g–h). This suggests that both the *Mw* 6.8 and *Mw* 6.0 aftershocks that occurred in the same day as the mainshock are probably a result of static stress triggering. The triggering relationship with the last event of the sequences that occurred 3 months later, however, seems to be controlled

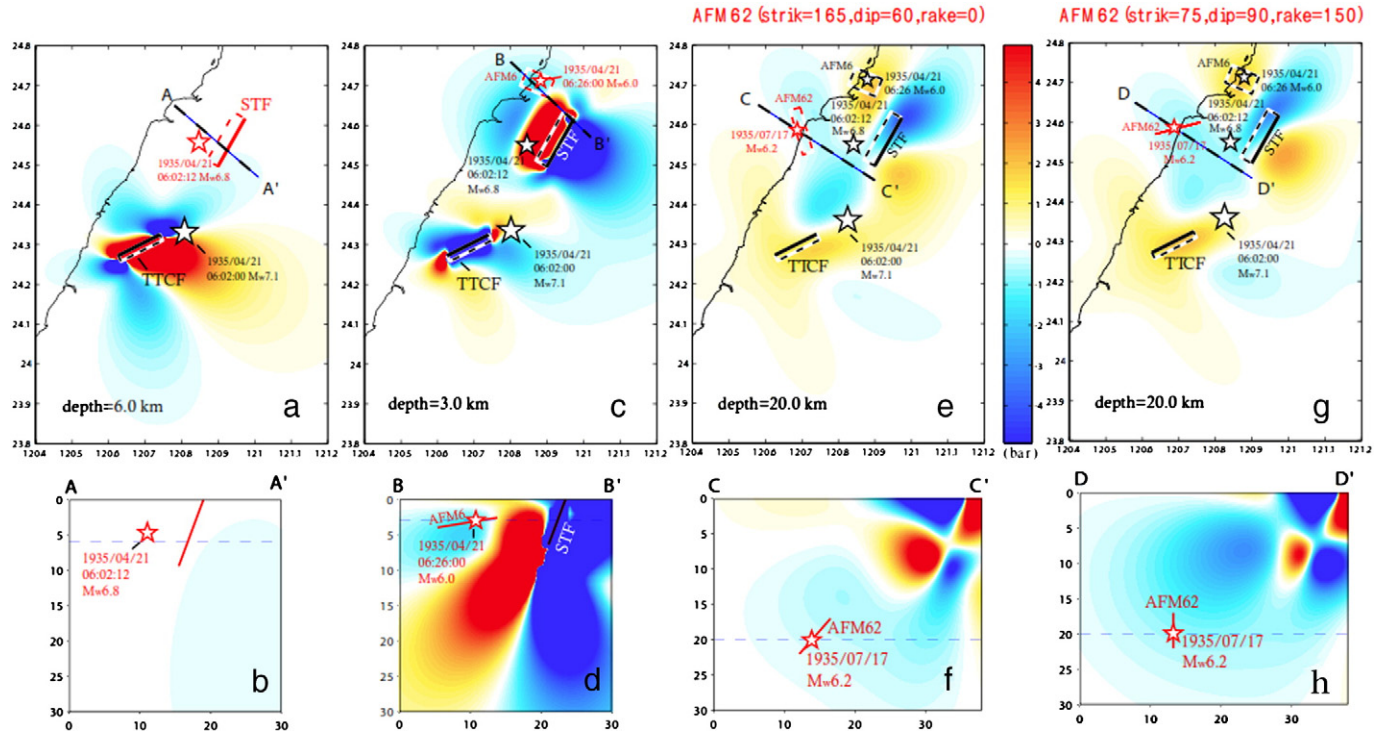

Fig. 6. Cumulative Coulomb stress changes caused by major events in the 1935 earthquake sequence resolved on the fault plane of subsequent ruptures using Model A (see Table S1 in the Supplementary material for fault parameters used). (a) Coulomb stress changes at a depth of 6 km due to the seismic displacement of TTCF rupture. (b) Cross-sectional area across A–A' in (a). Black line in mapview denotes the surface projection of fault model applied to calculate stress calculation. Red line and star denote the next rupture and epicenter/hypocenter. (c) Coulomb stress changes at a depth of 3 km due to the displacement of the TTCF and STF ruptures. (d) Cross-sectional area across profile B–B' in (c). (e, g) Coulomb stress changes resolved on the last July 17 *Mw* 6.2 aftershock at a depth of 20 km for two possible fault planes. (f) Cross-sectional area across profiles C–C' in (e). (h) Cross-sectional area across profiles D–D' in (g). Horizontal dashed lines in cross sections indicate the target depth determined by the focal depth of the next rupture events. μ is assumed to be 0.8 for (a,b,c,d) because STF and AFM6 were thrust faults, while μ is 0.4 for (e, f, g, h) due to the strike slip faulting of the July 17 *Mw* 6.2 aftershock.

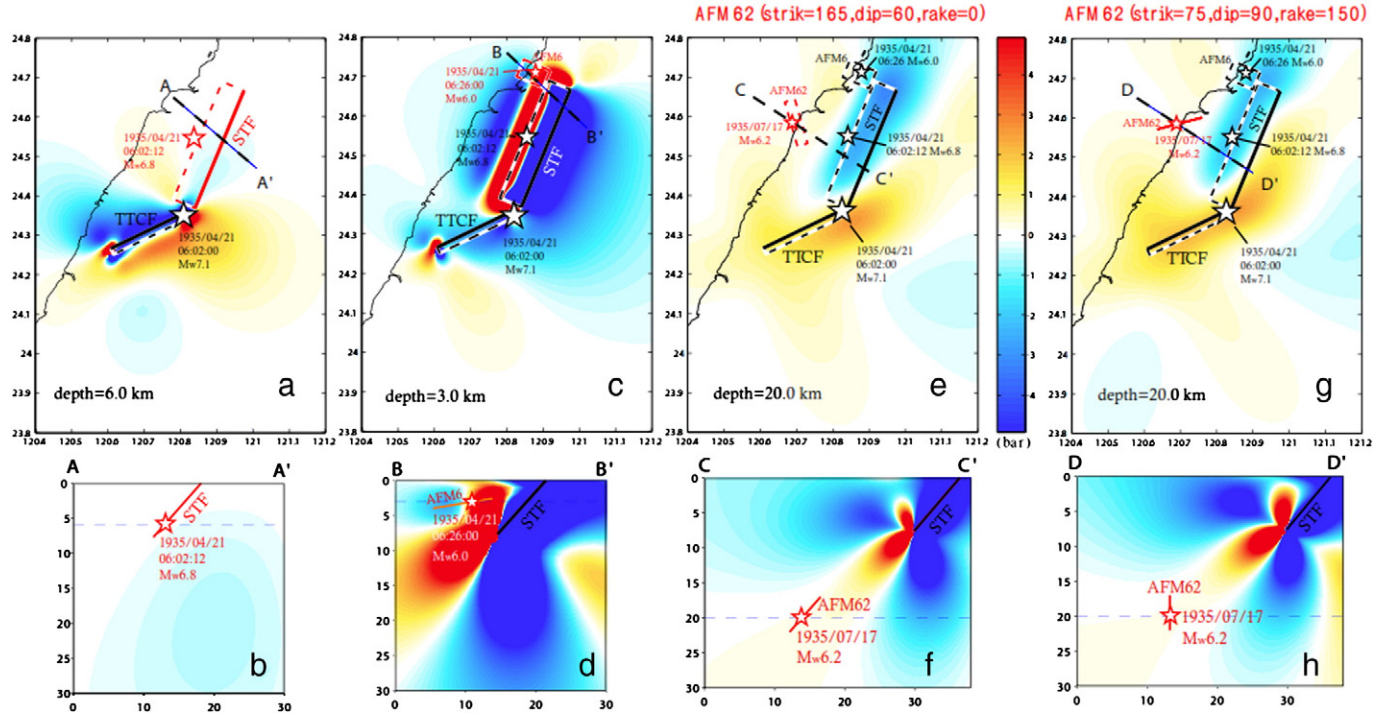

Fig. 7. Same with Fig. 6 but the cumulative Coulomb stress changes are resolved using Model B (see Table S1 in the Supplementary material for fault parameters used).

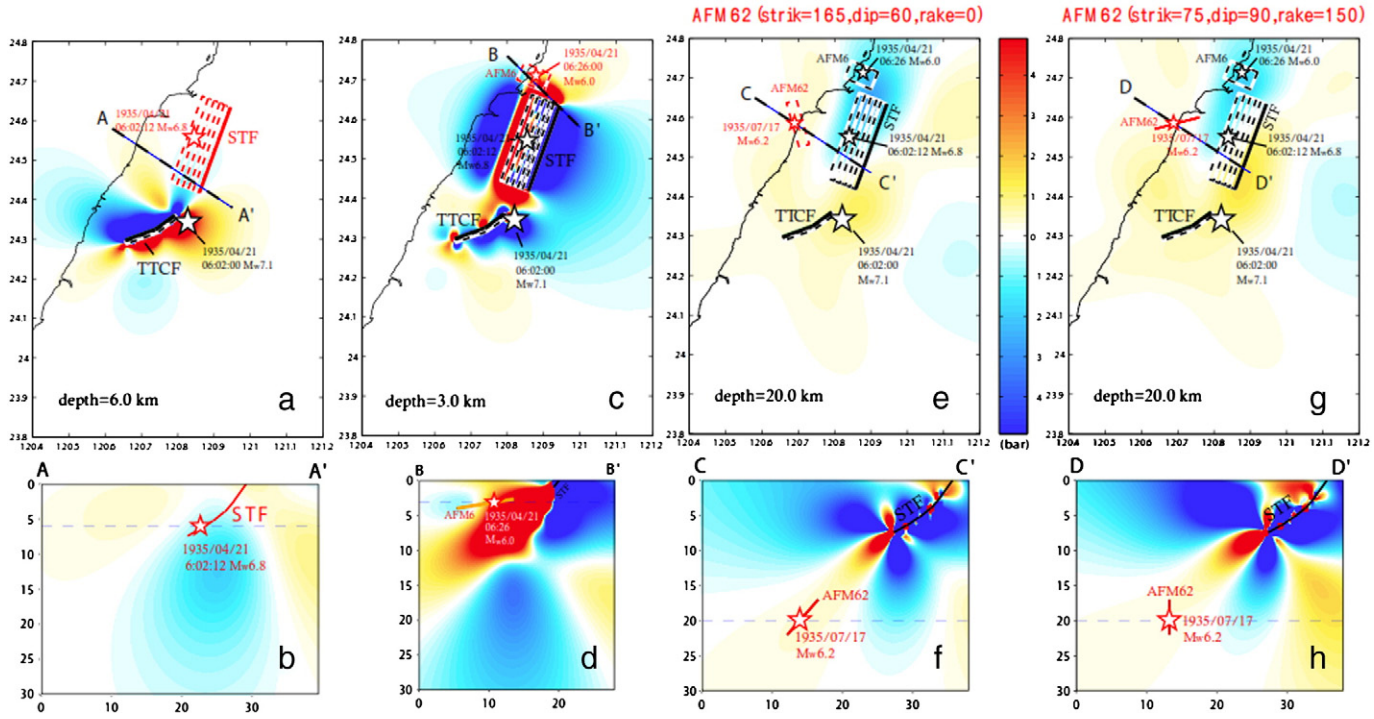

Fig. 8. Same with Fig. 6 but the cumulative Coulomb stress changes are resolved using Model C (see Table S1 in the Supplementary material for fault parameters used).

by the dip angle of the STF or STBF. This can be shown by the visual comparison of Figs. 6f to 10f. If the auxiliary fault plane of AFM6 is considered, the correlation between stress changes and sequential ruptures remain similar, as shown in Figs. S4 to S8 in the Supplementary material. A series of stress calculation indicates that the static stress transfer appears to advance slip on the subsequent $Mw > 6.0$ events at the same day when the blind fault(s) are considered.

7. Discussion

7.1. Short-term earthquake triggering

Most likely, dynamic triggering, static trigging, or a transient increase of creep rate plays a role in short-term triggering. The time lag of 12 s between TTCF and STF ruptures is in a range of time where

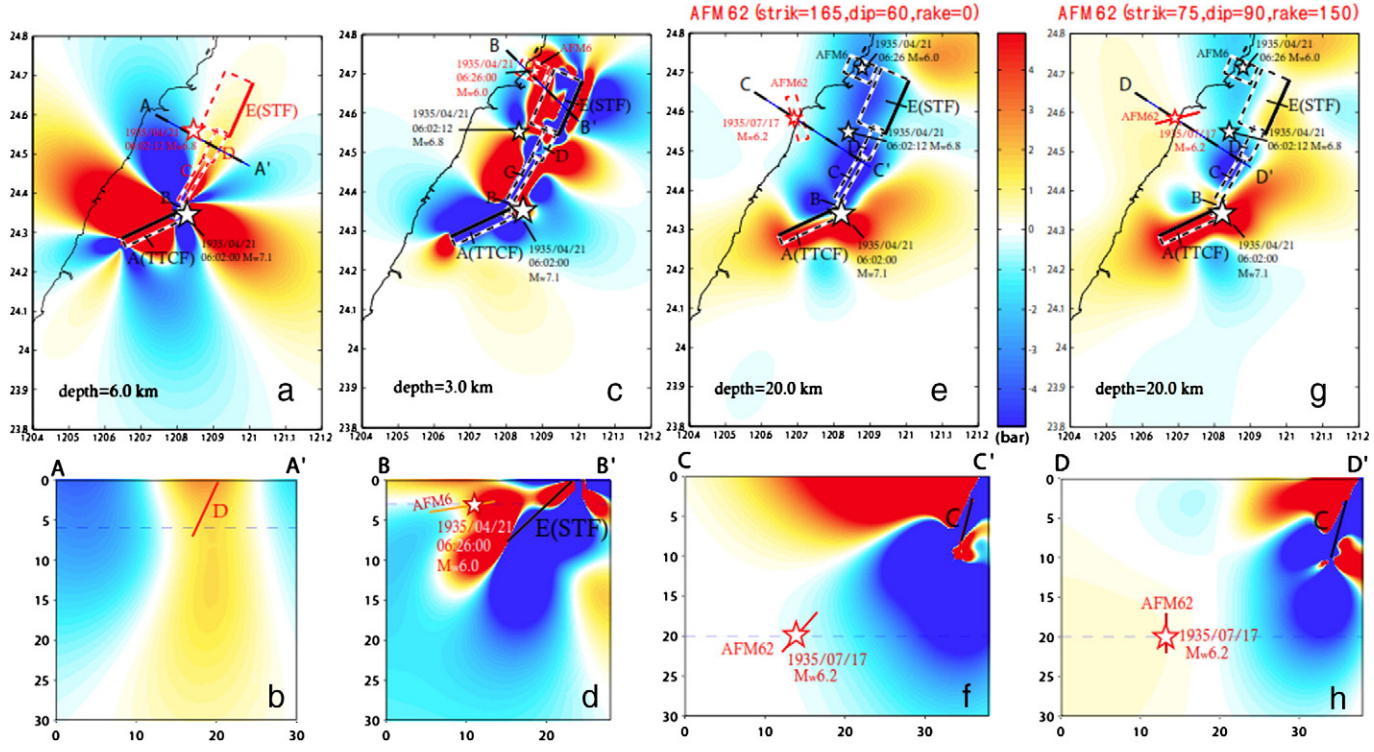

Fig. 9. Same with Fig. 6 but the cumulative Coulomb stress changes are resolved using Model D (see Table S1 in the Supplementary material for fault parameters used).

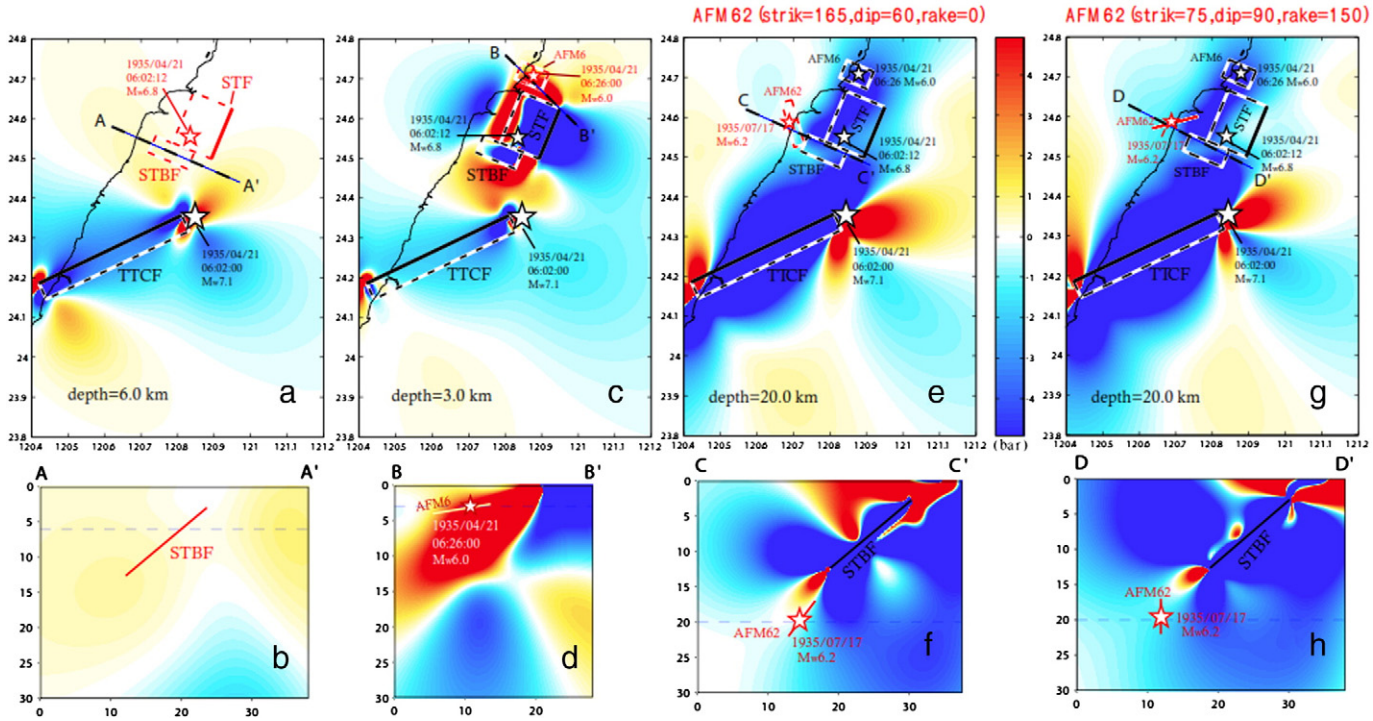

Fig. 10. Same with Fig. 6 but the cumulative Coulomb stress changes are resolved using Model E (see Table S1 in the Supplementary material for fault parameters used).

elastic waves arrived, suggesting that dynamic stress interaction is possible. However, there was only one seismic station near the 1935 event (Fig. S1 in the Supplementary material), making the dynamic stress modeling difficult. Increase of creep rate after the mainshock rupture, viscoelastic relaxation, and fluid migration are also possible, but no available data that allow us to confirm or rule out this possibility. Therefore, we cannot differentiate static stress triggering from other mechanisms, nor make a statement that the static stress triggering is the key parameter to confine which fault model is more accurate than the others. We have however discussed the effects from a range of uncertainties on static stress model, and tested the hypothesis whether or not Coulomb stress change would promote or inhibit subsequent ruptures.

The stress evolution using the previous three models (Models A to C) does not produce good correlation between the subsequent rupture and the static stress distribution. Since the unexposed segment of STF is evident by (1) large deformation in between the surface ruptures of TTCF and STF (from triangulation and leveling data), (2) minor surface faults, landslides, and fissure in between the two ruptures (from surface investigation). Together with the fact that initial rupture point of STF took place at the bottom of the fault (from rupture histories computed from seismic wave simulation), Models D and E are likely the better models. Model D contain two segments of unexposed STF, where they have quite different strike, dip, and rake with the main STF segment. Such a model supported by the geomorphologic evidences, however, is too complicated to be a preferred model in seismic hazard assessment application. Therefore we prefer Model E for the understanding of stress interaction between 1935 sequential ruptures.

7.2. Problems of static stress model

Coulomb stress model relies heavily on the assumption of earthquakes taking place on fault planes when stress reaches a critical failure state. The computation requires the unknown static earthquake slip in an elastic half-space, and later the earthquake induced stress changes are resolved on receiver fault using Eq. (4). The basic Coulomb failure criterion leads to some arguments for the predictive power for regional seismicity. For example, Woessner et al. (2011) evaluates performances of eleven statistical (ETAS and STEP models) and physical-based (Coulomb stress change and rate-state friction model) forecasting models on the 1992 Landers sequence. They argued that Coulomb stress change should be resolved on the 3-D optimally oriented planes other than specific receiver fault for forecasting purpose.

Here we detail the problems in the use of the static stress model and provide possible solutions for future studies. (1) *Static Coulomb stress change calculation cannot explain the temporal triggering effect*. Adding a temporal dimension to fault friction using the rate/state friction model (*Dieterich*, 1994) will improve our understanding of temporal evolution of seismicity, where the "rate" indicates rate at which the fault slips and the "state" denotes the physical properties of the fault surface. In the rate/state friction model, time-dependent seismicity rate is a result of a sudden stress step induced by a large earthquake (static stress change determined in this study) and the time elapsed since the last event. The decay rate depends on fault properties and the loading condition, which we need a precise measures of background seismicity rate and aftershock decaying pattern. However, the TTCF and STF have been quiet since the 1935 events so that the statistically meaningful estimate of background seismicity and aftershock duration is not available at this moment. (2) *Visual correlation between positive Coulomb stress change and aftershocks (or next major events) could be biased*. Uncertainties in source location and receiver fault parameters exist especially for historical earthquakes that did not have precise seismic and geodetic network as a constraint. Such uncertainties therefore, result in uncertainties in the computed stress change. Sensitivity test on a range of uncertain fault parameters should help, to examine the robustness of the static stress triggering model. (3) *Friction changes largely over time*. The Coulomb failure criterion assumes that the coefficient of friction does not change with time. However, it is widely discovered that coefficient of friction is time and velocity dependent (Dieterich, 1978; Ruina, 1983). Laboratory experiments demonstrate that coefficient of friction decreases roughly as the inverse of the sliding velocity V for $V > 0.1$ m/s (Beeler et al., 2008; Hirose and Shimamoto, 2005;

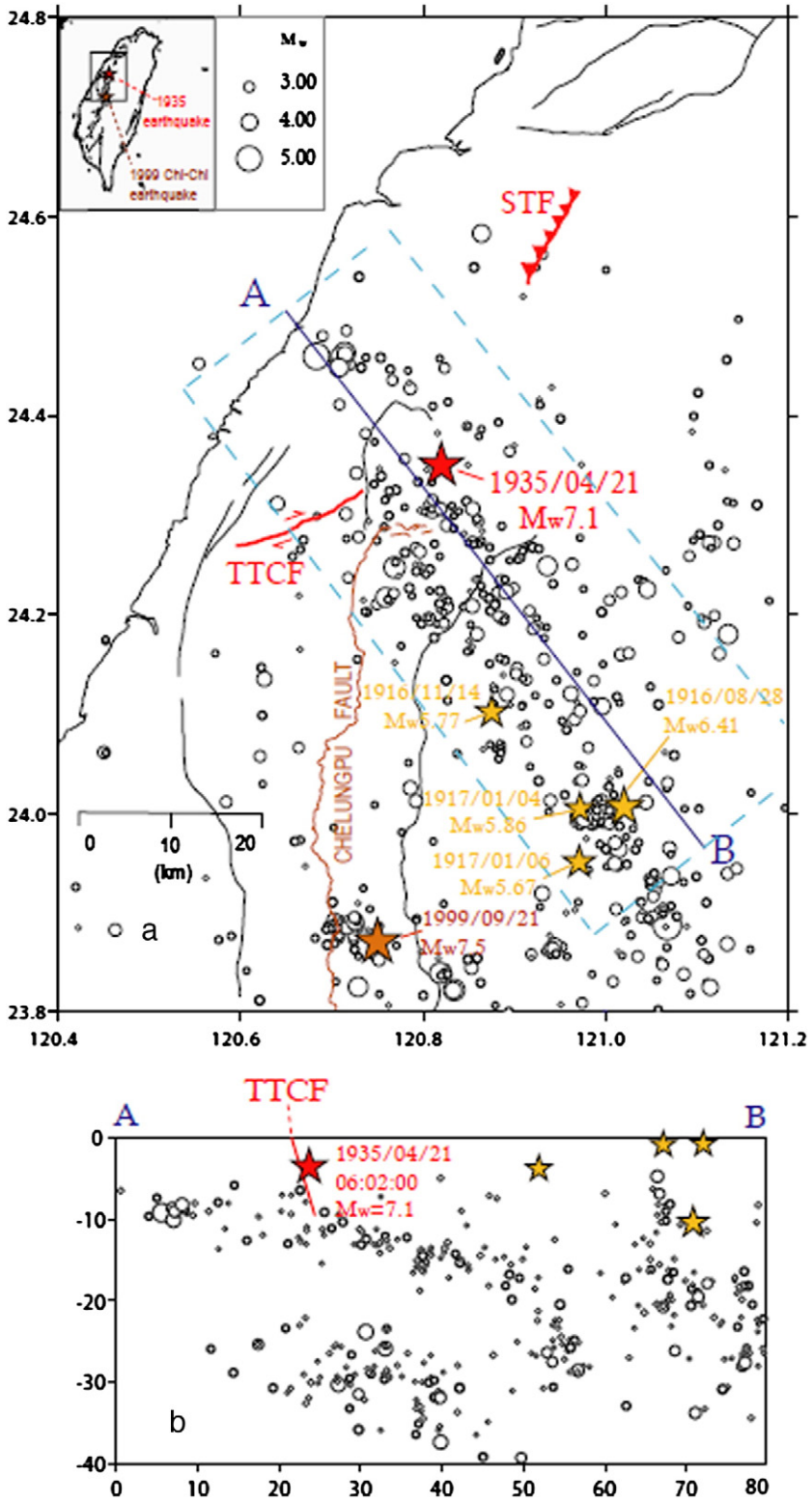

Fig. 11. (a) Relocated 2.5 ≦ *Mw* < 6.0 seismicity from January 01, 1991 to September 20, 1999 (before the 1999 Chi-Chi *Mw* 7.6 earthquake) in northwest Taiwan. Red star and lines denote the 1935 mainshock and two ruptures (STF and TTCF), respectively. Yellow stars denote the historical *M* > 5 events. A linear NW-trending zone from Sanyi to Puli is the Sanyi–Puli seismic zone (80 km long) (Wu and Rau, 1998). Along-strike cross-section A–B illustrate the depth extent of Sanyi–Puli seismic zone to be 40 km.

Tsutsumi and Shimamoto, 1997). Di Toro et al. (2004) also found that during earthquake cycle, coefficient of friction can change from 0.6 (during the loading) to near 0 (during high-velocity seismic slip). Such large variation in friction is likely a result of thermal weakening process including lubrication by hydrous films coating the gouge particles (Reches and Lockner, 2010; Sammis et al., 2011), silica gel formation (Goldsby and Tullis, 2002), formation of hotpots and macroscopic streaks of melt (Brown and Fialko, 2012), and thermal decomposition (Han et al., 2007). Earthquake simulation on the other hand, illustrates that for mature faults that experienced significant

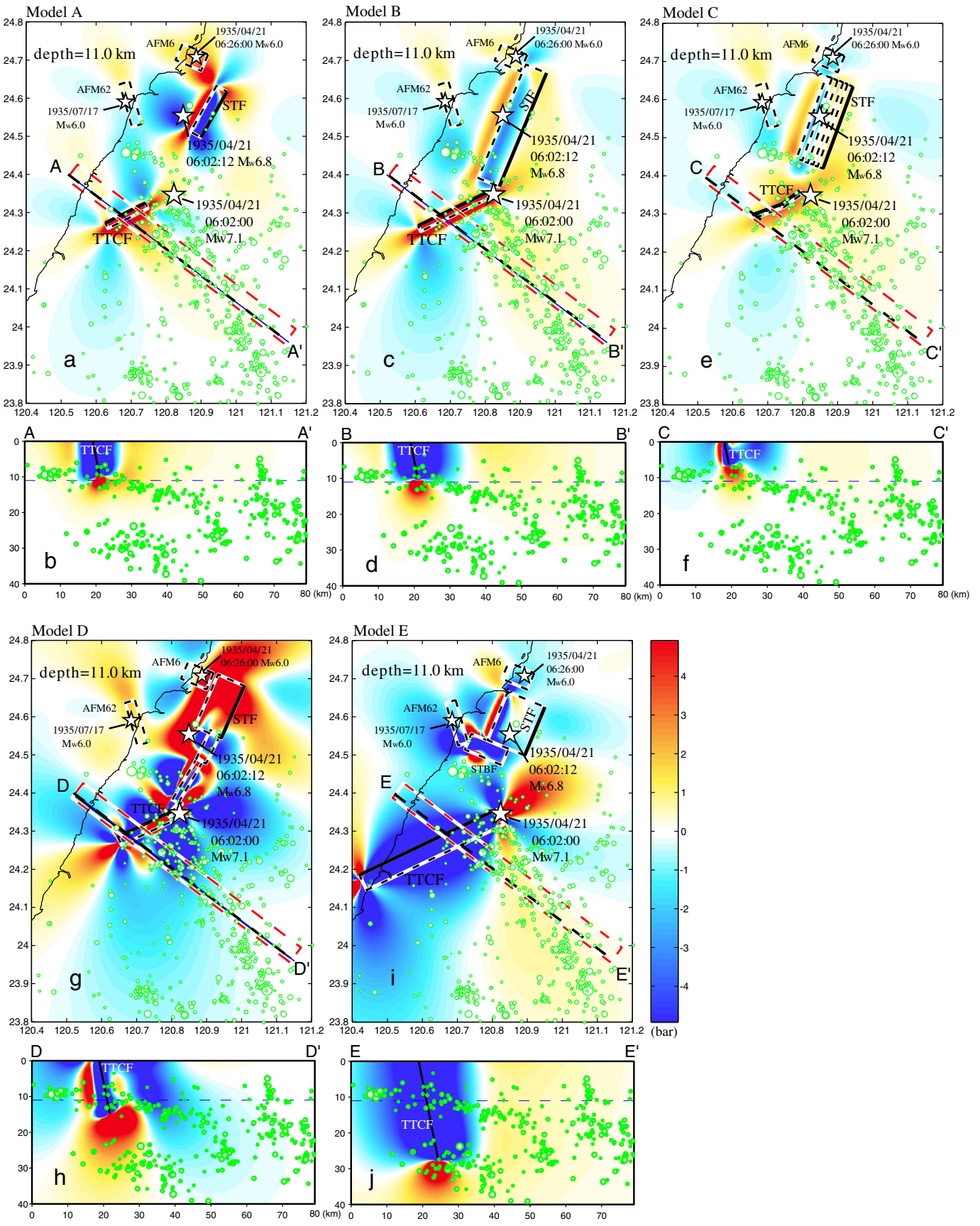

Fig. 12. Coulomb stress changes resolved on the fault plane of the Sanyi–Puli seismic zone (receiver fault: strike 307°, dip 80°, rake 0° by Rau et al., 1996) using the five models in Table 2. (a, c, e, g, i) Coulomb stress changes induced by the 1935 events at a depth of 11 km. (b, d, f, h, j) Cross-sectional area along the Sanyi–Puli seismic zone. Open red circles indicate the 1991 to 1999 seismicity. Here μ is assumed to be 0.4 determined by the strike-slip receiver fault of the Sanyi–Puli seismic zone.

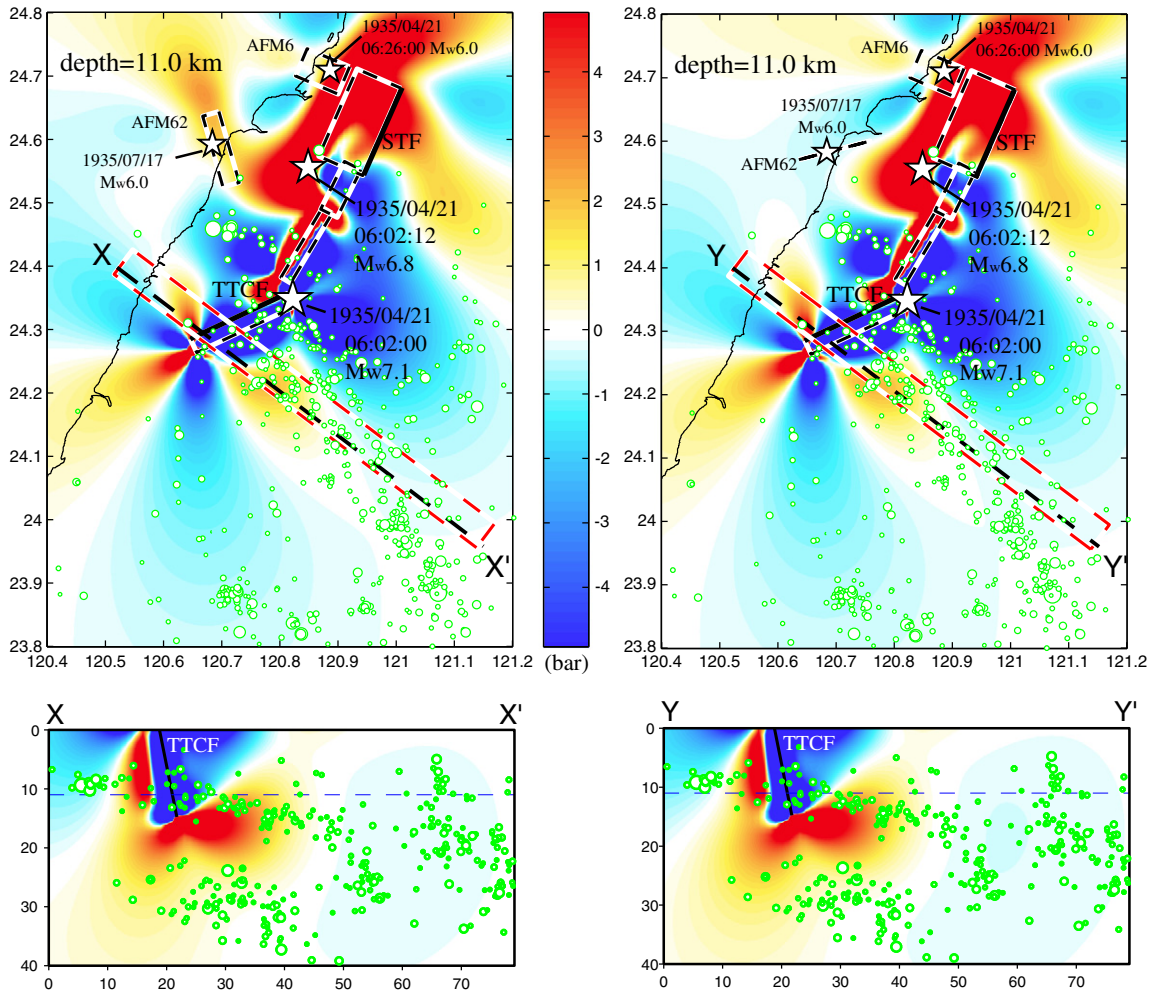

Fig. 13. Coulomb stress changes resolved on the fault plane of the Sanyi–Puli seismic zone using Model D without segment of TTCF (B) in Table 2. Two fault planes are considered for the AFM62.

slips and near yield stress, the friction and slip velocity tend to increase when additional stress applied (Lapusta and Barbot, 2012).

7.3. Other possible mechanisms for earthquake triggering

Due to the limited information provided by seismic and geodetic data for the 1935 sequence, this study concentrates solely on the concept of static stress transfer. There are other triggering mechanisms remain to be discussed. For the 1935 sequence, both viscoelastic triggering and dynamic stress transfer are possible. A viscous process is commonly used to explain the temporal correlations between major earthquakes over a large span of time (e.g., Freed and Lin, 2001; Pollitz et al., 1998). However, long-delayed triggering is not the specific feature in the 1935 sequence. On the other hand, if dynamic stress triggering is the major mechanism, one expects to see the next rupture in line with the directivity following the wave train (Gomberg et al., 2003). However, the poor seismic station coverage leads to the measurement of peak dynamic stresses associated

Table 4
Coulomb stress changes on sequential ruptures.

	Model A	Model B	Model C	Model D	Model E
Stress on STF	−0.09	−0.13	−0.17	5.50 (on STF-C) 1.80 (on STF-D) 0.48 (on STF-E) 2.59 (average)	0.03 (on STF) 0.41 (on STBF)
Stress on AFM6	−1.40	−0.35	1.34	3.36	4.42
Stress on AFM62 (1)	−0.45	0.20	0.36	−0.26	−0.15
Stress on AFM62 (2)	−0.79	0.18	0.29	0.27	−1.93
Stress on Sanyi–Puli (with AFM62 (1))	0.15	0.19	0.12	−2.26 0.72 (without TTCF-B)	0.92
Stress on Sanyi–Puli (with AFM62 (2))	0.13	0.17	0.10	−2.30 0.68 (without TTCF-B)	0.90

Unit in bars.

with passing seismic waves for the 1935 H-T sequence difficult. Therefore, whether dynamic stress transfer contributes to the triggering behavior is still an unknown. Fluids can play a major role in earthquake triggering due to the fluid flow induced pore-pressure variation (Brodsky et al., 2000; Nur and Booker, 1972; Prejean et al., 2004; Sleep and Blanpied, 1992). Swarm-like sequence or migration of time-clustered earthquake can be the indicator of fluid induced triggering. However, it is hard to resolve this possibility based on the poor resolution of earthquakes location during the 1935 sequence.

7.4. Seismic potential posed by a hidden fault

Blind thrusts can trigger slip on secondary faults in the shallow crust and meanwhile, produce aftershocks over a broad area (Lin and Stein, 2004). Based on computation on static stress change, Lin and Stein (2004) and Toda (2008) argue that the blind thrust does not need to be long, to trigger the rupture of adjacent faults with a comparable size. The 1935 earthquake sequence indeed provides another example of earthquake triggering by a blind thrust.

After the 1935 events, the 1935 source area has been characterized by very few earthquakes over the past decades. The frequent seismicity, however, occurs in the south of the TTCF and forms a linear zone called the Sanyi–Puli seismic zone. This linear seismic zone with a total length of ~70 km was noticed by 1991 to 1997 Central Weather Bureau Seismic Network seismicity map (Wu and Rau, 1998). Using 500 relocated $2.5 \leqq M < 6.0$ earthquakes from January 1, 1991 to September 20, 1999 (before the *Mw* 7.6 Chi-Chi earthquake), we show the spatial relationship between the 1935 earthquake sequence and the Sanyi–Puli seismic zone in Fig. 11. The NW–SE trending Sanyi–Puli seismic zone extends from Sanyi to Puli across the 1935 *Mw* 7.1 mainshock epicenter, nearly perpendicular to the strike of TTCF and STF. Given that the Sanyi–Puli zone was primarily active prior to the Chi-Chi earthquake (i.e., the next major event to shock central Taiwan after 1935). Given that the Sanyi–Puli seismic zone extends substantially deeper than the brittle-ductile transition, Wu and Rau (1998) inferred that anomalous high strain rates or rheological changes may be taking place here. The electrical structure (Chen and Chen, 2002) showed that metamorphic dehydration may trigger the active seismicity in this zone.

To understand if the regional stress responding to the 1935 earthquake sequence has some influence on this NW-trending seismic zone, we model the effect of the 1935 ruptures on the Sanyi–Puli seismic zone in Fig. 12. Focal mechanisms of small-to-moderate-sized earthquakes (Rau et al., 1996) and geomorphic evidence (Deffontaines et al., 1994) give the possible fault parameters for the Sanyi–Puli zone (strike = 307°, dip = 80°, rake = 0°), which is regarded as the receiver fault. The Coulomb stress changes using different fault models in Table 2 illustrate a common NW-trending stress increased lobe extending from the north end of the TTCF to Puli, consistent with the 1991–1999 seismicity patterns along the Sanyi–Puli zone. The only exception is the Model D. Using Model D, such a NW-trending lobe disappear while most stress concentration taking place toward north of STF. Such stress shadow is found to be due to the normal faulting segment of TTCF in Model D. As shown in Fig. 13 and Table 4 that without that small segment, the increased stress level is similar to that predicted from other fault models. Therefore we argue that with or without an unexposed fault segment involved in the stress computation, the 1935 earthquake sequence induced stress increases (0.1–0.9 bars) promoted the activity of the NW-trending seismic zone. This suggests that it is possible for the enhanced stress concentration due to the 1935 ruptures to play a role in the activity along the NW-trending zone. However, a better understanding of postseismic stress changes process (i.e., fault zone collapse, afterslip, and poroelastic rebound) is needed, to explain the delay times in the triggering process. This study provides a basis for further postseismic stress change calculations.

8. Conclusions

This study shows that static stress changes appear useful in explaining the triggering of sequential ruptures during the 1935 Hsinchu–Taichung earthquake sequence in central Taiwan. Specifically, we tested stress interactions among four major $M > 6.0$ events that occurred within 3 months using three different fault models proposed by early studies based on inversion of geodetic and seismic waveform data. Computing the Coulomb stress change induced by coseismic displacement from the mainshock on the TTCF, we found that the second rupture on the STF would fall in the stress increased region only if an unexposed segment(s) located between TTCF and STF is considered. The *Mw* 6.04 event that occurred 24 min after the mainshock was likely triggered by the faulting of both TTCF and STF ruptures, where the influence of a blind fault is less significant. A series of stress calculation indicates that the static stress transfer appears to advance slip on the subsequent major events ($Mw > 6.0$) and $Mw > 3.0$ aftershocks when the unexposed segment STBF is considered. The existence of the blind fault, therefore, is likely to play a significant role in the earthquake triggering process in this area. This blind fault segment may need our attention for future large earthquake potential in this area. We also discuss the seismic potential posed by the 1935 earthquake sequence considering solely elastic responses to fault slip. By the Coulomb stress analysis, we find that the lobes of increased Coulomb stress changes coincide with a NW–SE trending Sanyi–Puli seismic zone. The stress transfer model presented here raises the possibility that stress adjustment effect from the 1935 earthquake sequence may play a role in the present Sanyi–Puli seismic zone, and meanwhile, serves as a basis for future study on viscoelastic modeling of postseismic stress changes.

Acknowledgments

We thank the Seismological Center of Central Weather Bureau of Taiwan for the earthquake data. Figures were generated using the Generic Mapping Tools (GMT), developed by Wessel and Smith (1991). This research was partially supported by Taiwan NSC grant 101-2116-M-006-003.

Appendix A. Supplementary data

Supplementary data to this article can be found online at http://dx.doi.org/10.1016/j.tecto.2013.04.022.

References

Anderson, J.G., Brune, J.N., Louie, J.N., Zeng, Y., Savage, M., Yu, G., Chen, Q., dePolo, D., 1994. Seismicity in the western Great Basin apparently triggered by the Landers, California, earthquake, 28 June 1992. Bulletin of the Seismological Society of America 84, 863–891.

Angelier, J., Barrier, E., Chu, H.T., 1986. Plate collision and paleostress trajectories in a fold-thrust belt: the foothills of Taiwan. Tectonophysics 125, 161–178.

Beeler, N.M., Tullis, T.E., Goldsby, D.L., 2008. Constitutive relationships and physical basis of fault strength due to flash heating. Journal of Geophysical Research 113, B01401. http://dx.doi.org/10.1029/2007JB004988.

Brodsky, E.E., Karakostas, V., Kanamori, H., 2000. A new observation of dynamically immerged regional seismicity: earthquakes in Greece following the August, 1999 Izmit, Turkey earthquake. Geophysical Research Letters 27, 2741–2744.

Brown, K.M., Fialko, Y., 2012. 'Melt welt' mechanism of extreme weakening of gabbro at seismic slip rates. Nature 638 (488). http://dx.doi.org/10.1038/nature11370.

Byerlee, J., 1978. Friction of rocks. Pure and Applied Geophysics 116, 615–626.

Chen, C.C., Chen, C.S., 2002. Sanyi–Puli conductivity anomaly in NW Taiwan and its implication for the tectonics of the 1999 Chi-Chi earthquake. Geophysical Research Letters 29 (8), 1166. http://dx.doi.org/10.1029/2001GL013890.

Chen, K.P., Tsai, Y.B., 2008. A catalog of Taiwan earthquakes (1900–2006) with homogenized M_w magnitudes. Bulletin of the Seismological Society of America 98, 483–489. http://dx.doi.org/10.1785/0120070136.

Cheng, S.N., 1995. The Study of Stress Distribution in and Around Taiwan. Ph.D. Thesis National Central University, Chungli, Taiwan (215 pp. (in Chinese with English abstract)).

Das, S., Scholz, C.H., 1981. Off-fault aftershock clusters caused by shear stress increase? Bulletin of the Seismological Society of America 71, 1669–1675.

Deffontaines, B., Lee, J.C., Angelier, J., Carvalho, J., Rudant, J.P., 1994. New geomorphic data on the active Taiwan orogen: a multisource approach. Journal of Geophysical Research 99, 20,243–20,266.
Di Toro, G., Goldsby, D.L., Tullis, T.E., 2004. Friction falls towards zero in quartz rock as slip velocity approaches seismic rates. Nature 427, 436–439.
Dieterich, J.H., 1978. Time-dependent friction and the mechanics of stick-slip. Pure and Applied Geophysics 116, 790–806.
Dieterich, J.H., 1994. A constitutive law for rate of earthquake production and its application to earthquake clustering. Journal of Geophysical Research 99, 2601–2618.
Dieterich, J.H., Kilgore, B., 1996. Implications of fault constitutive properties for earthquake prediction. Proceedings of the National Academy of Sciences of the United States of America 93, 3787–3794.
ERI (Earthquake Research Institute), 1936. Field investigation. Bulletin of the Earthquake Research Institute, University of Tokyo, Part II, Reports. (Suppl. 3), 156–193 (in Japanese).
Freed, A.M., Lin, J., 2001. Delayed triggering of the 1999 Hector Mine earthquake by viscoelastic stress transfer. Nature 411, 180–183.
Goldsby, D., Tullis, T., 2002. Low frictional strength of quartz rocks at subseismic slip rates. Geophysical Research Letters 29 (17), 1844. http://dx.doi.org/10.1029/2002GL015240.
Gomberg, J., Bodin, P., 1994. Triggering of the Ms = 5.4 Little Skull Mountain, Nevada, earthquake with dynamic strain. Bulletin of the Seismological Society of America 84, 844–853.
Gomberg, J., Blanpied, M.L., Beeler, N.M., 1997. Transient triggering of near and distant earthquakes. Bulletin of the Seismological Society of America 87, 294–309.
Gomberg, J., Beeler, N., Blanpied, M., 2000. On rate-state and Coulomb failure models. Journal of Geophysical Research 105, 7857–7872.
Gomberg, J., Reasenberg, P.A., Bodin, P., Harris, R.A., 2001. Earthquake triggering by seismic waves following the Landers and Hector Mine earthquakes. Nature 411, 462–466.
Gomberg, J., Bodin, P., Reasenberg, P., 2003. Observing earthquakes triggered in the near field by dynamic deformations. Bulletin of the Seismological Society of America 93, 118–138.
Han, R., Shimamoto, T., Hirose, T., Ree, J.-H., Ando, J., 2007. Ultralow friction of carbonate faults caused by thermal decomposition. Science 316, 878–881.
Hanks, T.C., Kanamori, H., 1979. A moment magnitude scale. Journal of Geophysical Research 84, 2348–2350.
Harris, R.A., 1998. Introduction to special section: stress triggers, stress shadows, and implication for seismic hazard. Journal of Geophysical Research 103, 24,347–24,358.
Harris, R.A., Simpson, R.W., 1998. Suppression of large earthquakes by stress shadows: a comparison of Coulomb and rate-and-state failure. Journal of Geophysical Research 103, 24,439–24,451.
Hill, D.P., Reasenberg, P.A., Michael, A., Arabaz, W.J., Beroza, G.C., 1993. Seismicity remotely triggered by the magnitude 7.3 Landers, California, earthquake. Science 260, 1617–1623.
Hirose, T., Shimamoto, T., 2005. Growth of a molten zone as a mechanism of slip weakening of simulated faults in gabbro during frictional melting. Journal of Geophysical Research 110, B05202. http://dx.doi.org/10.1029/2004JB003207.
Hsu, M.T., 1971. Seismicity of Taiwan and some related problems. Bulletin of the International Institute of Seismology and Earthquake Engineering 8, 41–160.
Hu, J.-C., Angelier, J., Lee, J.-C., Chu, H.-T., Byrne, D., 1996. Kinematics of convergence, deformation and stress distribution in the Taiwan collision area: 2-D finite-element numerical modeling. Tectonophysics 255, 243–268.
Huang, B.S., Yeh, Y.T., 1992. Source geometry and slip distribution of the April 21, 1935 Hsinchu–Taichung, Taiwan earthquake. Tectonophysics 210, 77–90.
Hukunaga, M., Sato, M., 1938. Crustal deformations in central Taiwan, part 1. Bulletin of the Earthquake Research Institute, University of Tokyo 16, 300–316.
Kilb, D., 2012. A strong correlation between induced peak dynamic Coulomb stress change from the 1992 M 7.3 Landers, California, earthquake and the hypocenter of the 1999 M 7.1 Hector Mine, California, earthquake. Journal of Geophysical Research 108 (B1). http://dx.doi.org/10.1029/2001JB000678.
Kilb, D., Gomberg, J., Bodin, P., 2000. Earthquake triggering by dynamic stresses. Nature 408, 570–574.
King, G.C.P., Stein, R.S., Lin, J., 1994. Static stress changes and the triggering of earthquakes. Bulletin of the Seismological Society of America 84, 935–953.
Lai, Y.C., Huang, B.S., Yen, H.Y., Chen, K.C., 2004. Reexamination for seismic observations of the 1935 and 1941 Taiwan earthquake series based on modern techniques and new earth model. EOS. Transactions of the American Geophysical Union 85 (28) (Western Pacific Geophysics Meeting Suppl., Abstract. S31A-21).
Lapusta, N., Barbot, S., 2012. Models of earthquakes and aseismic slip based on laboratory-derived rate-and-state friction laws. In: Bizzarri, A., Bhat, H.S. (Eds.), The Mechanics of Faulting: From Laboratory to Real Earthquakes. Research Signpost, Kerala, India, pp. 153–207.
Lee, J.-C., Chu, H.-T., Angelier, J., Chan, Y.-C., Hu, J.-C., Lu, C.-Y., Rau, R.-J., 2002. Geometry and structure of northern surface ruptures of the 1999 Mw = 7.6 Chi-Chi, Taiwan earthquake: influence from inherited fold belt structures. Journal of Structural Geology 24, 173–192.
Lin, D.H., 1987. Mechanism of the Hsinchu–Taichung, Taiwan, Earthquake of 1935. M.S. Thesis National Central University, Chungli, Taiwan (88 pp. (in Chinese with English abstract)).
Lin, Y.N., 2005. Surface Deformation and Seismogenic Structure Model of the 1935 Hsinchu–Taichung Earthquake (M_{GR} = 7.1), in Miaoli, Northwestern Taiwan. Master Thesis National Taiwan University (77 pp.).
Lin, J., Stein, R.S., 2004. Stress triggering in thrust and subduction earthquakes and stress interaction between the southern San Andreas and nearby thrust and strike-slip faults. Journal of Geophysical Research 109, B02303. http://dx.doi.org/10.1029/2003JB002607.
Lin, C.W., Chang, H.C., Lu, S.T., Shih, T.S., Huang, W.J., 2000. An introduction to the active faults of Taiwan (second edition): explanatory text of the active fault map of Taiwan, Scale 1:500,000. Central Geological Survey Special Publication 13, 122pp. (in Chinese with English abstract).
Military Land Survey, 1937. Report of Revision Surveys of 1st, 2nd and 3rd Order Triangulations and 1st Order Precise Leveling in the Taiwan Earthquake Zone (8 pp. (in Japanese)).
Miyabe, N., Hukunaga, M., Sato, M., 1938. Crustal deformations in central Taiwan, part 2. Bulletin of the Earthquake Research Institute, University of Tokyo 16, 579–596.
Nur, A., Booker, J.R., 1972. Aftershocks caused by pore fluid flow? Science 275, 885–887.
Oppenheimer, D.H., Reasenberg, P.A., Simpson, R.W., 1988. Fault plane solutions for the 1984 Morgan Hill, California, earthquake sequence: evidence for the state of stress on the Calaveras fault. Journal of Geophysical Research 93, 9007–9026.
Otuka, Y., 1936. The earthquake of central Taiwan (Formosa), April 21, 1935, and earthquake faults. Bulletin of the Earthquake Research Institute, University of Tokyo (Suppl. 3), 22–74 (in Japanese with English abstract).
Parsons, T., Stein, R.S., Simpson, R.W., Reasenberg, P.A., 1999. Stress sensitivity of fault seismicity: a comparison between limited-offset oblique and major strike-slip faults. Journal of Geophysical Research 104, 20183–20202.
Pollitz, F.F., Bürgmann, R., Romanowicz, B., 1998. Viscosity of oceanic asthenosphere inferred from remote triggering of earthquakes. Science 280, 1245–1249.
Prejean, S., et al., 2004. Remotely triggered seismicity on the United States west coast following the M7.9 Denali Fault earthquake. Bulletin of the Seismological Society of America 94 (6B), S348–S359.
Rau, R.-J., Wu, F.T., Shin, T.C., 1996. Regional network focal mechanism determination using 3-D velocity model and SH/P amplitude ratio. Bulletin of the Seismological Society of America 86, 1270–1283.
Reches, Z., Lockner, D.A., 2010. Fault weakening and earthquake instability by powder lubrication. Nature 467, 452–455.
Ruina, A., 1983. Slip instability and state variable friction laws. Journal of Geophysical Research 88, 10,359–10,370.
Sammis, C., Lockner, D., Reches, Z., 2011. The role of adsorbed water on the friction of a layer of submicron particles. Pure and Applied Geophysics 168, 2325–2334.
Seno, T., Stein, S., Gripp, A.E., 1993. A mode for the motion of the Philippine Sea plate consistent with NUVEL-1 and geological data. Journal of Geophysical Research 98, 17,941–17,948.
Sheu, H.C., Kosuga, M., Sato, H., 1982. Mechanism and fault model of the Hsinchu–Taichung (Taiwan) earthquake of 1935. Zisin 2 (35), 567–574 (in Japanese).
Shin, T.C., 1986. Duration-magnitude correction for Taiwan Telemetered Seismographic Network. Bulletin of the Institute of Earth Sciences, Academia Sinica 6, 109–120.
Shyu, J.B.H., Sieh, K., Chen, Y.G., Liu, C.S., 2005. Neotectonic architecture of Taiwan and its implications for future large earthquakes. Journal of Geophysical Research 110, B08402. http://dx.doi.org/10.1029/2004JB003251.
Sleep, N., Blanpied, M.L., 1992. Creep, compaction and the weak rheology of major faults. Nature 359, 687–692.
Smith, S.W., Van de Lindt, W., 1969. Strain adjustments associated with earthquakes in southern California. Bulletin of the Seismological Society of America 59, 1569–1589.
Stein, R.S., 1999. The role of stress transfer in earthquake occurrence. Nature 402, 605–609.
Stein, R.S., Lisowski, M., 1983. The 1979 Homestead Valley earthquake sequence, California: control of aftershocks and postseismic deformation. Journal of Geophysical Research 88, 6477–6490.
Stein, R.S., Barka, A.A., Dieterich, J.H., 1997. Progressive failure on the North Anatolian fault since 1939 by earthquake stress triggering. Geophysical Journal International 128, 594–604.
Suppe, J., 1981. Mechanics of mountain building and metamorphism in Taiwan. Memoir of the Geological Society of China 4, 67–89.
Suppe, J., 2007. Absolute fault and crustal strength from wedge tapers. Geology 35, 1127–1130.
Teng, L.S., 1990. Geotectonic evolution of Late Cenozoic arc-continent collision in Taiwan. Tectonophysics 183, 57–76.
TMO (Taipei Meteorological Observatory), 1936. The Report of the April 21st, 1935, Hsinchu–Taichung Earthquake. Taipei Meteorological Observatory (160 pp. (in Japanese)).
Toda, S., 2008. Coulomb stresses imparted by the 25 March 2007 Mw = 6.6 Noto-Hanto, Japan, earthquake explain its 'butterfly' distribution of aftershocks and suggest a heightened seismic hazard. Earth Planets Space 60, 1041–1046.
Toda, S., Stein, R.S., 2003. Toggling of seismicity by the 1997 Kagoshima earthquake couplet: a demonstration of time-dependent stress transfer. Journal of Geophysical Research 108, 2567. http://dx.doi.org/10.1029/2003JB002527.
Toda, S., Stein, R.S., Richards-Dinger, K., Bozkurt, S., 2005. Forecasting the evolution of seismicity in southern California: animations built on earthquake stress transfer. Journal of Geophysical Research 110, B05S16. http://dx.doi.org/10.1029/2004JB003415.
Tsutsumi, A., Shimamoto, T., 1997. High-velocity frictional properties of gabbro. Geophysical Research Letters 24 (6), 699–702.
Voisin, C., Cotton, F., Di Carli, S., 2004. A unified model for dynamic and static stress triggering of aftershocks, antishocks, remote seismicity, creep events, and multisegmented rupture. Journal of Geophysical Research 109, B06304. http://dx.doi.org/10.1029/2003JB002886.
Wessel, P., Smith, W., 1991. Free software helps map and display data. EOS. Transactions of the American Geophysical Union 72 (441), 445–446.
Woessner, J., et al., 2011. A retrospective comparative forecast test on the 1992 Landers sequence. Journal of Geophysical Research 116, B05305. http://dx.doi.org/10.1029/2010JB007846.
Wu, F.T., Rau, R.-J., 1998. Seismotectonics and identification of potential seismic source zones in Taiwan. Terrestrial, Atmospheric and Oceanic Sciences 9, 739–754.
Yeh, Y.Y., Ou, G.B., Lin, C.C., 1982. Determination of local magnitude scale for Taiwan. Bulletin of the Institute of Earth Sciences, Academia Sinica 2, 37–48.
Yu, S.B., Chen, H.Y., Kuo, L.C., 1997. Velocity field of GPS stations in the Taiwan area. Tectonophysics 274 (1–3), 41–59.